Geochemistry, Geophysics, Geosystems

RESEARCH ARTICLE
10.1029/2020GC009358

Key Points:

- Rhyolitic glass inclusions indicate the early Bishop magma reservoir had a δD value of −40‰ to −60‰
- Inclusions lack evidence for isotopic fractionation
- The isotopic signature of Bishop Tuff rhyolite is most similar to arc basalts

Correspondence to:
K. S. Befus,
Kenneth_Befus@Baylor.edu

Citation:
Befus, K. S., Walowski, K. J., Hervig, R. L., & Cullen, J. T. (2020). Hydrogen isotope composition of a large silicic magma reservoir preserved in quartz-hosted glass inclusions of the Bishop Tuff Plinian eruption. *Geochemistry, Geophysics, Geosystems*, *21*, e2020GC009358. https://doi.org/10.1029/2020GC009358

Received 10 AUG 2020
Accepted 31 OCT 2020

Hydrogen Isotope Composition of a Large Silicic Magma Reservoir Preserved in Quartz-Hosted Glass Inclusions of the Bishop Tuff Plinian Eruption

Kenneth S. Befus[1], Kristina J. Walowski[2], Richard L. Hervig[3], and Jeffrey T. Cullen[4]

[1]Department of Geosciences, Baylor University, Waco, TX, USA, [2]Geology Department, Western Washington University, Bellingham, WA, USA, [3]School of Earth and Space Exploration, Arizona State University, Tempe, AZ, USA, [4]Jackson School of Geosciences, University of Texas at Austin, Austin, TX, USA

Abstract Water controls magmatic crystallization and drives volcanic eruptions, but little is known about its primary source in silicic systems. The hydrogen isotope composition of volcanic products provides a metric that can track and identify magmatic source, fractionation, or degassing processes. Despite such promise, hydrogen isotope measurements have never previously been acquired for undegassed silicic melt. To explore whether hydrogen isotopes can identify the source and modification of water in a silicic magma reservoir, we analyzed D/H ratios and dissolved H_2O content of quartz-hosted, rhyolitic glass inclusions from the early Bishop Tuff, a time-honored testing ground for innovative petrologic studies. The rhyolitic inclusions indicate the early Bishop reservoir had δD values ranging from −40‰ to −60‰ (Vienna Standard Mean Ocean Water). The measured hydrogen isotope ratios do not follow systematic trends that would be predicted for open-system degassing, rehydration, or diffusive loss. Observed isotopic variability in the microanalyses is instead attributed to analytical artifacts. The large silicic reservoir degassed as a closed system, resulting in limited fractionation obscured by the uncertainty of the measurements. Significant modification of melt D/H ratios by assimilation and fractional crystallization are unlikely, as their projected contributions are not observed. Dynamic geologic processes are thus not recorded by the hydrogen isotope composition of the inclusions. Instead, the rhyolitic melt represents a distinct, largely homogenous isotopic reservoir. When compared to the global record of basaltic glass inclusions, the rhyolitic inclusions preserve an isotopic signature that is most similar to subduction-related mafic melts.

Plain Language Summary Water is always present in magma, dissolved at the molecular level. The amount of dissolved water controls how magma may erupt or crystallize in the subsurface. Identifying the behavior and primary source of the magmatic water is an important question, one that is commonly obscured by volcanic eruptions. To avoid a volcanic overprint, we studied small glass blebs of frozen magma that are entirely encapsulated in a protective jacket of quartz crystals. We measured the abundance of water isotopes, H and D, in those glasses. The glasses preserve a relatively high amount of D relative to H. This observation allows us to systematically eliminate various processes that could have changed the isotopic ratio of H to D in the magma. Bubbles formed in the magma, but the exsolved gas never escaped to the surface. We also conclude that the magma's hydrogen isotopes were not changed by crystallization or melting surrounding host rock. No changes mean the water's isotopes reflect its original source. The H and D preserved in the protected glassy parcels of frozen Bishop Tuff reveal the water is sourced from subduction zone processes.

1. Introduction

The crystal cargo of a magma provides an in situ record of magmatic volatiles and degassing. The stability of hydrous minerals, such as mica and amphibole, is dictated by the presence and fugacity of magmatic water. Minerals may also entrap small parcels of magma during crystal growth, preserved as glass inclusions. Following entrapment, the crystal host provides a protective jacket that ideally preserves the compositional integrity of the original melt during quenching to glass during eruption and emplacement. Major and trace element studies of such inclusions have transformed our understanding of preeruptive magmatic processes, having been used to explore crystallization processes, conduit ascent rates, and degassing (e.g., Blundy &

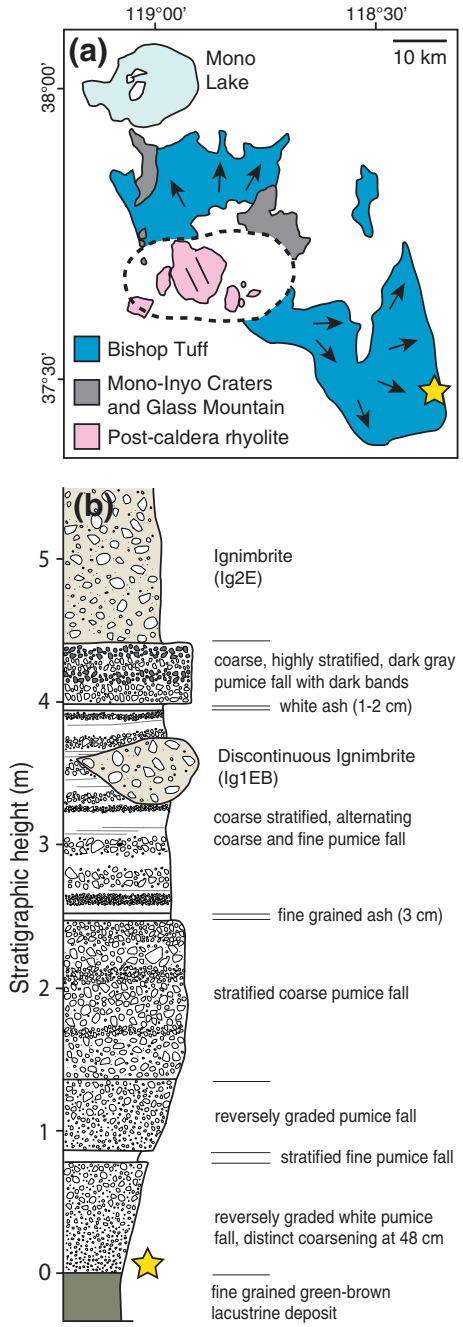

Figure 1. a) Regional geologic map of Long Valley Caldera in eastern California, United States, showing the sample location (star, at 37°27'38" N, 118°21'60" W) (modified from Wilson and Hildreth [1997]). (b) Schematic measured section of the Bishop Tuff at Chalfant Valley pumice quarry. Quartz crystals were collected from the lowest 8 cm of the basal fall (star).

Cashman, 2005; Dunbar & Hervig; 1992; Gaetani & Watson, 2002; Johnson et al., 2008). Glass inclusions can also retain the isotopic composition of the preeruptive magma at the moment of entrapment, which have been used to infer petrogenetic processes and contributions from subducting slabs, mantle sources, or crustal assimilates (e.g., Hauri, 2002; Saal et al., 1998; Shaw et al., 2008; Walowski et al., 2015). Most important for this contribution is that the initial preeruptive hydrogen isotope composition of a magma can be used to characterize the source of the magmatic water, and infer the tectonic processes that provide it. However, this preeruptive hydrogen isotope composition may be overprinted by fractionation caused by degassing (e.g., Newman et al., 1988; Taylor et al., 1983).

During degassing, the hydrogen isotope composition of a magma will move to more negative δD values as D preferentially partitions into the exsolved vapor, leaving a residual melt enriched in H (e.g., Dunbar & Kyle, 1992; Newman et al., 1988; Taylor et al., 1983). The systematic decrease in H_2O wt.% and D/H ratios documented in dense, glassy silicic pyroclasts is one of the best established petrologic records of eruptive degassing (Chaitén and Cordón Caulle [Castro et al., 2014]; Little Glass Mountain, Newberry Crater, Glass Creek [Taylor et al., 1983]; Mazama [Mandeville et al., 2009]; and Mono Craters [J. D. Barnes et al., 2014a; Newman et al., 1988]). This record has been explored using closed- and open-system degassing models to better understand the behavior of volatiles in the conduit environment, from the explosive onset to the effusive waning stages of an eruption (e.g., Rust et al., 2004). What more can we learn by looking deeper? Preeruptive degassing in the magma reservoir is known to occur, but the style and magnitude are difficult to constrain. The hydrogen isotope composition of glass inclusions may be used to discern if closed- or open-system behavior of the vapor operates in the reservoir. Because closed-system degassing produces little isotopic fractionation, an additional opportunity may exist to characterize the source of water in the magma reservoir using the relatively unaltered hydrogen isotope composition of the melt.

To investigate the source, behavior, and composition of water in a rhyolitic reservoir, we measured the hydrogen isotope composition of a suite of quartz-hosted rhyolitic glass inclusions from the early Bishop Tuff, Long Valley Caldera in eastern California, United States. The combined analyses of D/H (‰) and H_2O contents (wt.%) for a population of inclusions is the first such data set reported for a rhyolitic system, and the first report of D/H in quartz-hosted glass inclusions. We calibrate our measurements with a variety of natural and synthetic rhyolitic materials designed to mitigate matrix effects and analytical artifacts. Bishop Tuff inclusions are unmodified by magmatic degassing, diffusive loss, or assimilation-fractional crystallization processes. The hydrogen isotope composition of the rhyolitic Bishop Tuff is most comparable to basaltic glass inclusions from subduction zones worldwide.

2. Materials and Methods

2.1. Glass Inclusions

Quartz crystals were handpicked from a sample of loose, disaggregated pyroclastic fall collected from the lower 8 cm of the basal horizon of the Bishop Tuff at Chalfant Valley pumice quarry, Long Valley Caldera (Figure 1) (e.g., Wilson & Hildreth, 1997). The quartz was then submerged in mineral oil and inspected

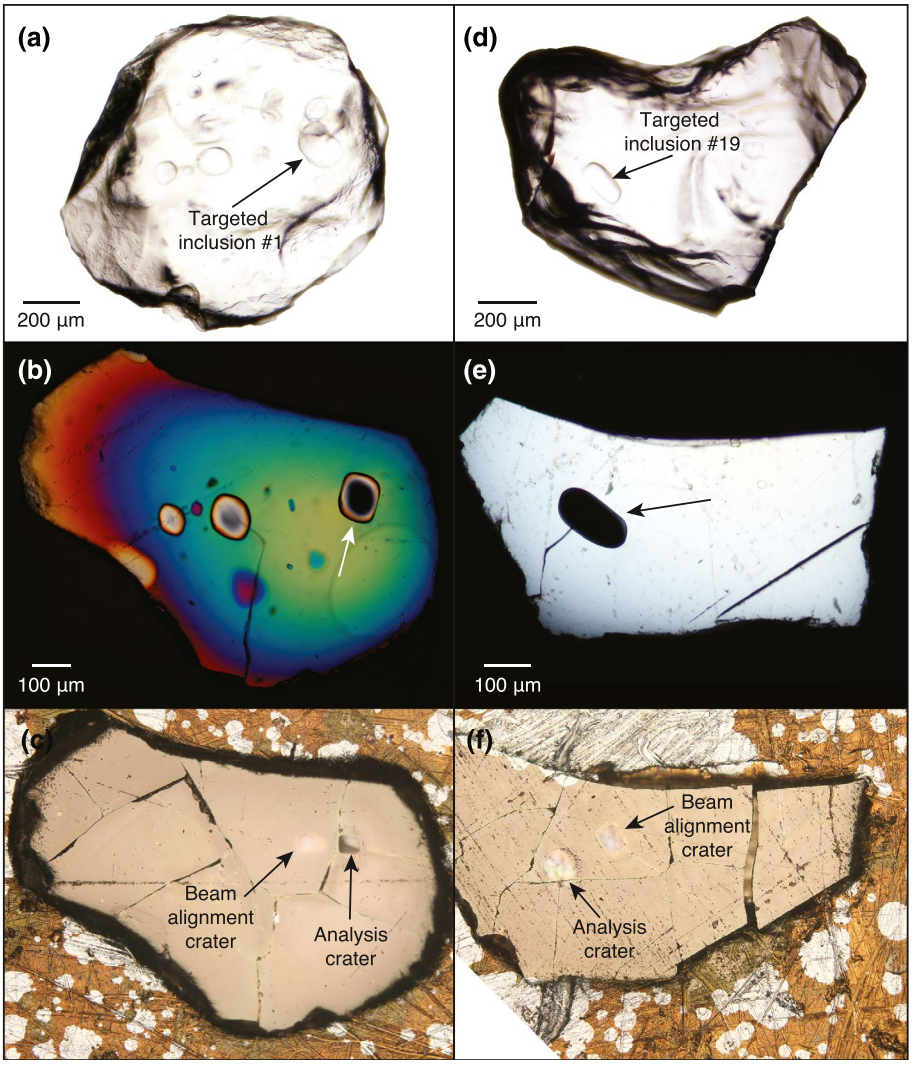

Figure 2. Photomicrographs of targeted quartz-hosted glass inclusions. Shown in plane light (a and d), cross polars with polished, doubly exposed inclusions (b and e), and reflected light when pressed in indium mount (c and f). Panels (a–c) are inclusion #1 and (d–f) are inclusion #19. Cracks in crystals were generated by sample preparation or pressing the crystal wafer into the indium.

with a binocular microscope. We selected a separate of quartz crystals containing polyhedral-shaped glass inclusions ≥40 µm in size, avoiding those containing vapor bubbles, crystallites, or intersected by cracks. The position and dimensions of each inclusion were measured optically. Analyzed inclusions were located 50–300 µm from the closest crystal face. The horizontal dimensions were measured using the binocular eyepiece reticle on an optical microscope, whereas the thickness of each inclusion (e.g., vertical dimension) was measured by focusing on the top and bottom of the inclusion using a petrographic microscope equipped with a Heidenhain focus linear drive encoder. Individual crystals that met the above specifications were mounted in Crystalbond, adhered to glass slides, and carefully polished to produce thin crystal wafers holding one or more doubly exposed, doubly polished inclusions (Figure 2). The inclusion-bearing quartz wafers were removed from the glass slides and the Crystalbond was removed by soaking in acetone and ethanol.

2.2. Experimental Glasses

We selected one synthetic and six natural rhyolitic glasses as calibration material for the hydrogen isotope measurements. Throughout the remainder of the manuscript we refer to these glasses as "standards,"

although we acknowledge that they have not been analyzed by multiple, independent laboratories, and that uncertainty remains regarding their spatial homogeneity. Iceland Deep Drilling Program (IDDP) is a hydrous rhyolite glass actively quenched during drilling of the Krafla, which contains ~2 wt.% H_2O and δD –114‰ ± 2‰ (Martin et al., 2017; Zierenberg et al., 2013). The North Mono Craters, CA, eruptions at 1325–1340 AD is the source for the remaining natural rhyolitic samples (Sieh & Bursik, 1986). The samples were collected and analyzed using Fourier-transform infrared (FTIR) and Thermal Conversion Elemental Analyzer (TC/EA) by J. D. Barnes et al. (2014a). P2N, P2D, and P10I are pyroclastic obsidian chips recovered from fall deposits associated with Panum Crater Dome, containing 1.9 ± 0.1, 1.2 ± 0.1, and 0.7 ± 0.1 wt.% H_2O and δD values of −62 ± 2, −69 ± 2, and −79‰ ± 2‰, respectively. PCD5 and NWC23 are obsidian collected from the effusive Panum Crater Dome and Northwest Coulee lavas. PCD5 contains 0.4 ± 0.1 wt.% H_2O and δD value of −101‰ ± 5‰, whereas NWC23 has 0.2 ± 0.1 wt.% H_2O and δD value of −97‰ ± 5‰ (J. D. Barnes et al., 2014a).

B24 is an experimental glass composed of hydrated rhyolite that was synthesized for this project. The starting material was an 86-mg cylinder of glass cored from a block of holohyaline, rhyolitic obsidian from North Coulee, Mono Craters. The glass initially contained ~0.2 wt.% H_2O and a hydrogen isotopic composition of ~−100‰. The glass cylinder was loaded into a 3-mm outside diameter Au capsule along with 6 mg of H_2O with a known isotopic composition of 0.8‰ (J.D. Barnes and T. Larson standard at University of Texas at Austin Stable Isotope Lab named "Kona"). The Au capsule was welded, shut and placed within a larger 5-mm O.D. Au capsule. The space between the capsules was packed with finely powdered dry rhyolite glass and then the larger capsule was welded shut. The pressurizing medium for the experimental system was water, which was continuously in contact with the Au capsule during the experiment. H diffuses orders of magnitude faster through gold than rhyolite melt. The purpose of the packed, outer dry rhyolite powder was to act as a sponge to absorb and prevent H from the pressurizing water penetrating into the inner experimental capsule. The experiment was performed by loading the capsule and a steel filler rod into an externally heated, cold-seal pressure vessel, and then inserted into a furnace. The experiment ran at 800°C and 270 MPa for 6 days. Such conditions were chosen to ensure the melt was water undersaturated and to allow sufficient time for the D and H to diffusively equilibrate throughout the melt. The sample was quenched in ~1 min by removing the pressure vessel from the furnace, blowing on it with compressed air, and then submerging it in a bucket of water. The capsule was then removed and weighed. Finally, the experimental glass was removed and prepared for petrographic, spectroscopic, and isotopic analyses.

2.3. Analytical Techniques

The bulk hydrogen isotope ratio of B24 glass was measured using a TC/EA coupled to a ThermoElectron MAT253 Isotope Ratio mass spectrometer in continuous flow mode at UT-Austin following the methods of Sharp et al. (2001) and Cassel et al. (2012). Approximately, 7–10 mg of finely crushed material was enclosed in Ag foil capsules, dried under vacuum at 70°C for 24 h, and flushed with dry He gas within a zero-blank auto-sampler prior to analysis. Replicate aliquots of the sample were analyzed over the analytical session. The sample was calibrated using contemporaneous analyses of three internationally distributed hydrogen isotope standards: USGS 57, USGS 58, and NBS-22, as well as an internal volcanic glass standard, SN09052RW. Water content from the results of these TC/EA analyses is calculated from a linear calibration using the known wt.% H_2O contents of standards, USGS 57 (biotite) and USGS 58 (muscovite), the mass of materialized analyzed, and the corresponding signal intensities.

We measured the dissolved H_2O and CO_2 contents (wt.% and ppm, respectively) of the glass inclusions and rhyolite glass standards by FTIR spectroscopy using a Thermoelectron iN10. Spectra were collected in both the mid-IR and near-IR range. Concentrations of molecular and hydroxyl H_2O in the water-rich glass inclusions and rhyolite standards were determined from absorbances at ~5,200 and ~4,500 cm^{-1}, using the calibration of Zhang et al. (1997). CO_2 contents were determined in the glass inclusions using the absorbance at ~2,350 cm^{-1} with the modified Beer-Lambert law and an absorption coefficient of 1,214 ± 16 L $cm^{-1}{\cdot}mol^{-1}$ (Behrens et al., 2004). Each inclusion measurement consisted of 60 scans collected at a resolution of 4 cm^{-1} and a 40 × 40 μm spot size. Water in the water-poor rhyolite standards was determined using the Beer-Lambert law, absorbance at ~3,500 cm^{-1}, an absorption coefficient of 71 L $cm^{-1}{\cdot}mol^{-1}$, and a density of 2,350 $kg{\cdot}m^{-3}$. Rhyolite standards were analyzed using targeted spots and area maps. Spot analyses

consisted of 60 scans collected at a resolution of 4 cm^{-1}. Maps were collected using a step size of 50 or 100 μm to march across the sample, and then compiling the hundreds of individual analyses into a map. Map analyses used a spectral resolution of 8 cm^{-1}, 60 scans, and a 50 × 50 μm spot size.

After collection of FTIR spectra, the quartz and rhyolite glass wafers were mounted in indium metal for secondary-ion mass spectrometry (SIMS) analyses . The wafers were carefully arranged into the center hollow of a 1-inch aluminum round holder and pressed firmly with a vice to produce a flat surface. The surface of the sample and holder were gold coated prior to analysis.

The hydrogen isotope compositions of rhyolite standards and quartz-hosted glass inclusions were determined by analyzing D, H, and ^{16}O using the Cameca IMS 6F secondary-ion mass spectrometer at Arizona State University. All D/H ratios are reported in standard δD (‰) notation relative to Vienna Standard Mean Ocean Water. A focused primary beam of Cs^+ was accelerated to +10 keV at a current of 1–1.6 nA. The beam was focused to a spot ~25 μm in diameter and rastered over a square area of 35 × 35 μm^2. The sample was held at −5,000 V. Transfer optics and a small-field aperture (400 μm) were adjusted to allow collection of negative secondary ions solely from the central, circular 15-μm-diameter area of the sputtered crater. Sample charging was corrected with a normal-incidence electron gun, tuned using the technique described in Chen et al. (2013). Each analysis consisted of first obtaining a secondary-ion image for oxygen. Next, the position of the Cs^+ beam was adjusted to be centered on the secondary-ion optical axis. The field aperture was then inserted and the target area was presputtered for 4 min to remove surface hydrogen. The secondary magnet was cycled between the two hydrogen isotopes, counting H for 1 s and then D for 10 s. After 100 to 600 cycles the secondary magnet was re-set to count $^{16}O^-$ for 5 s. A typical analysis of 100 cycles took ~30 min to complete and attained a precision of ~10‰ (two standard errors of the mean). The 2σ (standard errors of the mean) uncertainties on rhyolite inclusions ranged from 3‰ to 13‰. Analysis of (presumably) dry quartz in the indium mount demonstrates the background chamber counts contribute 1% to the analyses of D/H values in the glass inclusion. Background contributions to the isotopic ratios are ~2‰, and are thus less than the 2σ uncertainty of the measurement and are not a significant source of uncertainty (e.g., J. J. Barnes et al., 2014b; Tartese et al., 2013).

The glasses and inclusions were measured during a 5-day analytical session. Standards were repeatedly analyzed throughout the session to calibrate and monitor any drift in calibration. Standards B24, P2N, P2D, and IDDP were used to establish the isotopic instrumental mass fractionation (e.g., "alpha," defined as $(D/H)_{SIMS}/(D/H)_{BULK}$) because their elevated water contents were most similar to the water-rich inclusions (Figure 3). The calibration shifted after the third day, after a minor adjustment to the electron gun settings. We report the "first" and "second" calibrations for D/H and H_2O. The instrumental mass fractionation factors for D/H were 1.1836 ± 0.0079 and 1.0831 ± 0.0055 for the first and second calibrations, respectively (Figures 3b and 3d). To convert SIMS H^-/O^- measurements to H_2O, a nonlinear second-order polynomial provides the best fit (Figures 3a and 3c). Projecting our best-fit polynomial calibrations to the more elevated water contents expected in Bishop Tuff glass inclusions generates unavoidable uncertainties of +0.3 and −0.4 wt.% H_2O in the first calibration and +0.3 and −0.2 wt.% H_2O in the second (Figure 3).

3. Results

3.1. Glass Inclusions

The quartz-hosted rhyolitic glass inclusions contain 4.2–5.8 wt.% H_2O and up to ~70 ppm CO_2 (see Table 2, Figure 4). Those volatile contents correspond with previously published values and are thus considered representative of the early Bishop Tuff melt. Neither the H_2O nor CO_2 contents correlate with the position of the inclusion within the host quartz.

The average hydrogen isotope composition of 28 quartz-hosted rhyolitic inclusions is −65‰ ± 15‰ (see Table 2, Figure 7). The inclusions present a spread of ~55‰, with δD ranging from −38‰ to −92‰. Values ranging from −40‰ to −60‰ are considered most representative for the early Bishop Tuff. δD does not correlate with the inclusion's position within the quartz host, nor does it show any relationship with FT-IR-derived H_2O content (Figure 7a). SIMS-derived H_2O displays a negative correlation with δD in both the first and second calibrations (Figure 7b). The analytical effects that produce these differences are further discussed in Section 4.1.

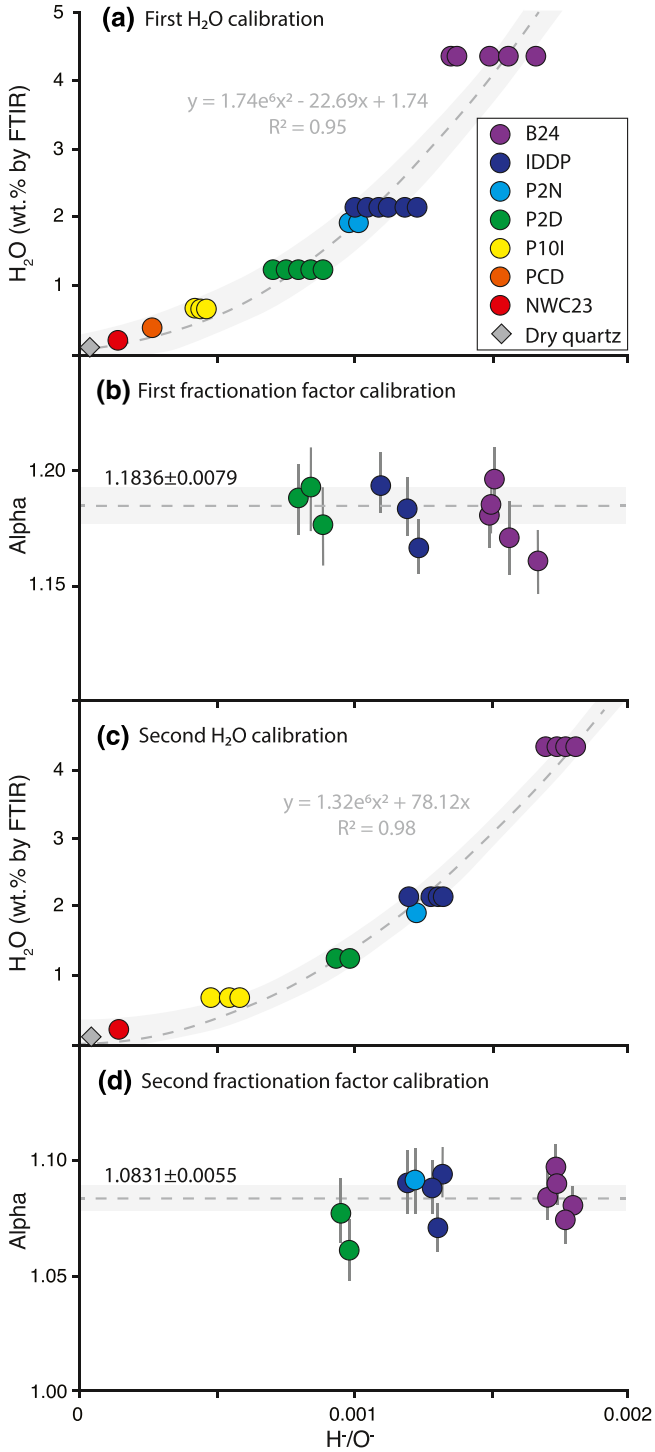

Figure 3. Calibration of H_2O and hydrogen isotope compositions for secondary-ion mass spectrometry (SIMS) analyses. The two calibrations are shown in (a and b) and (c and d), respectively. H_2O was calibrated using a nonlinear, second-order polynomial relationship between SIMS H^-/O^- and H_2O in standards established by Fourier-Tranform Infrared (a and c) Fractionation factor, or alpha, used to calculate the hydrogen isotope composition represents the average of the high-water standards (b and d). Error bars (2σ) are shown in gray when larger than symbol size. The uncertainty of the polynomial (1σ) and linear (2σ) regressions are similarly shown in light gray.

3.2. Experimental Glasses

The reliability of the glass inclusion isotopic compositions directly depends on the rhyolite calibration standards. As such, we carefully documented the textural, volatile, and isotopic homogeneity of each. B24, IDDP, P2D, and P10I are bubble-free, dense glass with sparse microlites and microphenocrysts (Figure 5). P2N, PCD5, and NWC23 contain vesicles that occupy 5–10 vol.% of the sample. Enriched and depleted volatile haloes generated by degassing or regassing may extend hundreds of micrometers from bubble margins in obsidian chips. The diameter of the modified halo corresponds closely to the size of the bubble (Watkins et al., 2012). To avoid potential isotopic fractionations associated with late-stage, eruptive processes, we targeted SIMS spots far from vesicles (approximately hundreds of micrometers).

The FTIR-derived H_2O content in each rhyolite glass matches the bulk measurement from TC/EA. The rhyolites are internally consistent in H_2O, with maximum relative variability ranging from 1% to 10% (Table 1). Where minor heterogeneity is observed, it presents spatially as gradients (P10I and B24), patches (P2D and IDDP), or bands (P2N) (Figure 5). SIMS-derived H_2O contents have much greater scatter than independent measurements with FTIR and TC/EA, but when the analyses are considered en masse, SIMS statistically reproduces the established H_2O contents (Figure 6a).

The bulk isotopic composition of the seven standards was established by TC/EA, and encompasses a wide range of δD values from +43‰ ± 2‰ to −114‰ ± 2‰ (J. D. Barnes et al., 2014a; Martin et al., 2017). However, the internal isotope homogeneity of these "standards" had not yet been explored. To mitigate this uncertainty, we spent more time analyzing the rhyolite glasses than quartz-hosted inclusions. Indeed, 48 out of the 76 SIMS analyses were performed on the rhyolite reference standards (Table 1). Of those, we focused primarily on the higher water content glasses (>1 wt.%) because they (B24, P2N, P2D, and IDDP) were most comparable to the inclusions. Those rhyolites display internal D/H variability <2% (by SIMS). Such consistent results, collected in dense glassy domains across the samples, suggest the rhyolites are reliable references that can be used to establish instrumental mass fractionation (particularly in the context of the samples that are the subject of this study). Conversely, our limited SIMS exploration of the rhyolites with <1 wt.% H_2O (P10I, PCD5, and NWC23) indicate that they fail to reproduce bulk δD determined by TC/EA. These drier rhyolites may be internally heterogeneous or require a different instrumental calibration. We do not consider them further. SIMS measurements of B24, P2N, P2D, and IDDP reproduce the bulk δD established by TC/EA when multiple analyses are considered as a population (Figure 6b). Single analyses can present variability ranging up to ∼30‰.

We include experimental glass B24 as one of our rhyolite standard materials. Three independent analyses of B24 glass chips by TC/EA are indistinguishable, recording a δD value +43‰ ± 2‰ and 4.3 wt.% H_2O in two runs, and +43‰ ± 2‰ and 4.2 wt.% H_2O in the other. Thus, the TC/EA measurement is 4.3 ± 0.1 wt.% H_2O and δD value of +43‰ ± 2‰ (1σ, $n = 3$). Averaged SIMS and FTIR reproduce these bulk values. The H_2O content and isotopic composition of B24 glass contains less-dissolved H_2O and more D relative to H than expected. Approximately 7 wt.% H_2O with an isotopic composition of 0.8‰ was added to the obsidian core in the inner Au capsule. We suggest that diffusive equilibration allowed H to diffuse from the inner capsule where it was incorporated by the interstitial rhyolite. As a result, the melt lost H_2O and became progressively enriched in D. Future standard synthesis may be able to account for this diffusive fractionation through Au capsule walls by adding water more enriched in H (e.g., δD ∼ −100‰) and buffering the intercapsule powder with D-enriched water. Experiment duration cannot be shortened because sufficient time is required to diffusively homogenize the melt.

4. Discussion

The Bishop Tuff is a meticulously studied series of interbedded pyroclastic fall and density current deposits (>600 km^3) produced by the 760 ka supereruption from Long Valley Caldera (Hildreth, 1979, 2004; Wilson & Hildreth, 1997). The units are commonly separated into an "early" and "late" petrologic classification that is based on rigorous temporal and compositional constraints, although that model has recently come under scrutiny because of assumptions regarding thermodynamic equilibrium, or lack thereof (e.g., Chamberlain et al., 2015; Evans et al., 2016; Gardner et al., 2014; Gualda & Ghiorso, 2013).

Table 1
Hydrogen Isotopic Composition and Volatile Contents of Rhyolite Glasses Used as Reference Standards

	FTIR	TC/EA	SIMS								
Sample	H_2O (wt.%)	Bulk δD (‰)	D/H	1σ	Alpha	H (cps)	O (cps)	H^-/O^-	H_2O (wt.%)	δD (‰)	2σ (‰)
B24_01	4.3 (0.1)	43 (2)	1.89E−04	1.11E−06	1.16 (0.01)	2.89E+05	1.72E+08	1.68E−03	4.7	22	12
B24_02			1.90E−04	1.30E−06	1.17 (0.02)	2.49E+05	1.58E+08	1.57E−03	4.1	31	14
B24_03			1.93E−04	9.38E−07	1.18 (0.01)	2.45E+05	1.63E+08	1.51E−03	3.8	43	10
B24_04			1.94E−04	1.19E−06	1.20 (0.02)	2.57E+05	1.69E+08	1.52E−03	3.8	53	12
B24_05			1.92E−04	1.08E−06	1.18 (0.01)	2.23E+05	1.49E+08	1.50E−03	3.7	40	11
B24_06			1.89E−04	9.75E−07	-	2.24E+05	1.43E+08	1.57E−03	4.1	22	10
B24_07			1.93E−04	1.07E−06	-	1.96E+05	1.30E+08	1.51E−03	3.8	44	11
B24_08			1.87E−04	8.67E−07	-	2.07E+05	1.32E+08	1.57E−03	4.1	15	9
B24_09			1.91E−04	8.86E−07	-	2.31E+05	1.53E+08	1.51E−03	3.8	34	9
B24_10			1.97E−04	9.00E−07	-	2.13E+05	1.54E+08	1.38E−03	3.2	65	9
B24_11			1.98E−04	9.05E−07	-	2.05E+05	1.50E+08	1.37E−03	3.1	75	9
B24_12[a]			1.78E−04	8.48E−07	1.10 (0.01)	2.90E+05	1.66E+08	1.74E−03	3.9	56	10
B24_13[a]			1.77E−04	7.48E−07	1.10 (0.01)	2.82E+05	1.62E+08	1.75E−03	3.9	49	8
B24_14[a]			1.76E−04	6.95E−07	1.08 (0.01)	2.99E+05	1.66E+08	1.80E−03	4.2	40	8
B24_15[a]			1.75E−04	7.98E−07	1.07 (0.01)	2.92E+05	1.64E+08	1.78E−03	4.0	34	9
B24_16[a]			1.76E−04	8.36E−07	1.08 (0.01)	2.80E+05	1.64E+08	1.71E−03	3.7	44	9
								B24 calibrated average	**3.9 (0.4)**	**42 (16)**	
IDDP_01	2.1 (0.1)	−114 (2)	1.61E−04	7.99E−07	1.17 (0.01)	2.38E+05	1.92E+08	1.24E−03	2.6	−126	10
IDDP_02			1.63E−04	8.80E−07	1.18 (0.01)	2.23E+05	1.86E+08	1.20E−03	2.4	−114	11
IDDP_03			1.65E−04	9.27E−07	1.19 (0.01)	1.92E+05	1.74E+08	1.10E−03	2.0	−106	11
IDDP_04			1.67E−04	9.14E−07	-	1.54E+05	1.46E+08	1.05E−03	1.9	−98	11
IDDP_05			1.62E−04	1.00E−06	-	1.62E+05	1.44E+08	1.13E−03	2.1	−122	12
IDDP_06			1.64E−04	9.67E−07	-	1.78E+05	1.62E+08	1.10E−03	2.0	−111	12
IDDP_07			1.68E−04	1.10E−06	-	1.71E+05	1.69E+08	1.01E−03	1.7	−90	13
IDDP_08[a]			1.50E−04	8.08E−07	1.09 (0.01)	2.31E+05	1.79E+08	1.29E−03	2.1	−110	11
IDDP_09[a]			1.51E−04	7.69E−07	1.09 (0.01)	2.37E+05	1.78E+08	1.33E−03	2.2	−105	10
IDDP_10[a]			1.48E−04	7.07E−07	1.07 (0.01)	2.43E+05	1.86E+08	1.31E−03	2.2	−124	10
IDDP_11[a]			1.51E−04	9.36E−07	1.09 (0.01)	2.08E+05	1.73E+08	1.20E−03	1.8	−108	12
								IDDP calibrated average	**2.1 (0.3)**	**−110 (11)**	
P2N_1	1.9 (0.04)	−62 (2)	1.79E−04	1.01E−06	-	2.33E+05	2.36E+08	9.90E−04	1.7	-32	11
P2N_2			1.77E−04	9.98E−07	-	1.92E+05	1.87E+08	1.03E−03	1.8	−42	11
P2N_3[a]			1.60E−04	1.06E−06	1.09 (0.01)	2.07E+05	1.68E+08	1.23E−03	1.9	−55	13
								P2N calibrated average	**1.8 (0.1)**	**−43 (12)**	
P2D_1	1.2 (0.1)	−69 (2)	1.71E−04	1.24E−06	1.18 (0.02)	1.35E+05	1.52E+08	8.90E−04	1.4	-75	15
P2D_2			1.73E−04	1.32E−06	1.19 (0.02)	1.14E+05	1.35E+08	8.49E−04	1.2	−62	15
P2D_3			1.72E−04	1.12E−06	1.19 (0.02)	1.19E+05	1.48E+08	8.07E−04	1.1	−66	13
P2D_4			1.76E−04	1.27E−06	-	9.32E+04	1.23E+08	7.61E−04	1.0	−46	14
P2D_5			1.78E−04	1.54E−06	-	1.01E+05	1.43E+08	7.07E−04	0.9	−35	17
P2D_6[a]			1.56E−04	1.15E−06	1.08 (0.02)	1.48E+05	1.54E+08	9.60E−04	1.1	−75	16
P2D_7[a]			1.54E−04	9.62E−07	1.06 (0.01)	1.55E+05	1.57E+08	9.88E-04	1.2	−88	12
								P2D calibrated average	**1.1 (0.2)**	**−64 (18)**	

Table 1
Continued

	FTIR	TC/EA	SIMS								
Sample	H_2O (wt.%)	Bulk δD (‰)	D/H	1σ	Alpha	H (cps)	O (cps)	H^-/O^-	H_2O (wt.%)	δD (‰)	2σ (‰)
P10I_1	0.7 (0.1)	−79 (2)	1.71E−04	1.39E−06	-	8.84E+04	1.99E+08	4.45E−04	0.4	−75	16
P10I_2			1.72E−04	1.38E−06	-	8.47E+04	1.96E+08	4.31E−04	0.4	−69	16
P10I_3			1.76E−04	7.18E−07	-	7.89E+04	1.73E+08	4.55E−04	0.4	−46	8
P10I_4			1.64E−04	1.40E−06	-	6.13E+04	1.32E+08	4.65E−04	0.4	−111	17
P10I_5[a]			1.58E−04	1.36E−06	-	8.27E+04	1.70E+08	4.88E−04	0.3	−62	17
P10I_6[a]			1.46E−04	1.78E−06	-	7.50E+04	1.28E+08	5.85E−04	0.4	−134	24
P10I_7[a]			1.44E−04	1.99E−06	-	6.02E+04	1.08E+08	5.59E−04	0.4	−145	28
P10I_8[a]			1.61E−04	1.49E−06	-	8.44E+04	1.77E+08	4.76E−04	0.3	−47	19
								P10I calibrated average	**0.4 (0.1)**	**−86 (39)**	
PCD5_1	0.4 (0.05)	−101 (5)	1.71E−04	1.08E−06	-	4.42E+04	1.62E+08	2.73E−04	0.2	−75	12
NWC23_1	0.2 (0.05)	−97 (5)	1.73E−04	1.11E−06	-	2.78E+04	2.29E+08	1.21E−04	0.2	−62	13
NWC23_2[a]			1.61E−04	2.83E−06	-	2.77E+04	1.89E+08	1.46E−04	0	−46	35
Quartz 68	-	-	1.65E−04	6.59E−06	-	4.00E+03	2.10E+08	1.90E−05	0	−105	80
Quartz 38[a]	-	-	1.57E−04	7.60E−05	-	2.79E+03	1.47E+08	1.89E−05	0	−75	967

Note. Values in parentheses represent 1σ standard deviation. "-" indicates not detected.
Abbreviations: FTIR, Fourier-transform infrared; TC/EA, Thermal Conversion Elemental Analyzer; SIMS, secondary-ion mass spectroscopy.
[a]Analyses in the second calibration.

Quartz-hosted glass inclusions have featured prominently in petrologic discussions of the Long Valley reservoir and a brief review places our hydrogen isotopic measurements in context. Extensive data sets demonstrate compositional bimodality, with the early Bishop Tuff inclusions containing ≤6 wt.% H_2O and ≤100 ppm CO_2 compared with ≤4.5 wt.% H_2O and ≤1,000 ppm CO_2 in the late Bishop Tuff inclusions (Anderson et al., 1989; Dunbar & Hervig, 1992; Peppard et al., 2001; Roberge et al., 2013; Skirius et al., 1990; Wallace et al., 1999). Major and trace element compositions of phenocrysts and glass from the early Bishop Tuff indicate that quartz-hosted inclusions were likely entrapped at 150–225 MPa and 720°C–820°C in the presence of a preeruptive exsolved fluid phase that comprised 1–6 wt.% (≤20 vol.%) (Bindeman & Valley, 2002; Gualda & Ghiorso, 2013; Wallace et al., 1995, 1999). Unlike the late-erupted Bishop Tuff quartz, early-erupted quartz crystals seldom preserve bright cathodoluminescent rims with high CO_2 inclusions (Gualda, 2007; Peppard et al., 2001; Roberge et al., 2013). Neither bright rims nor enriched CO_2 concentrations were observed in our inclusions or host quartz. The volatile contents of our sample suite correspond with previous studies, giving confidence that our analyzed inclusions are representative parcels of early Bishop Tuff melt (Figure 4, Table 2).

The early Bishop Tuff glass inclusions indicate that the Long Valley rhyolitic melt was a hydrogen isotopic reservoir with δD value of ∼−40‰ to −60‰. The observed δD within the data set of 28 individual inclusions ranges over ∼55‰. Long-duration SIMS analyses, comprised of 400–600 cycles, generate 2σ uncertainties <5‰ (Table 2). Such precision on individual inclusions, yet large range of δD, presents a challenging data set to confidently interpret. We use the following sections to explore the data set in the context of analytical uncertainties, viability of varied isotopic fractionations, and petrogenetic processes.

4.1. Analytical Considerations

Water contents as determined by FTIR represent the foundational observation for the glass inclusion data set. FTIR spot and map analyses of the standard rhyolite glasses correspond to the bulk water contents

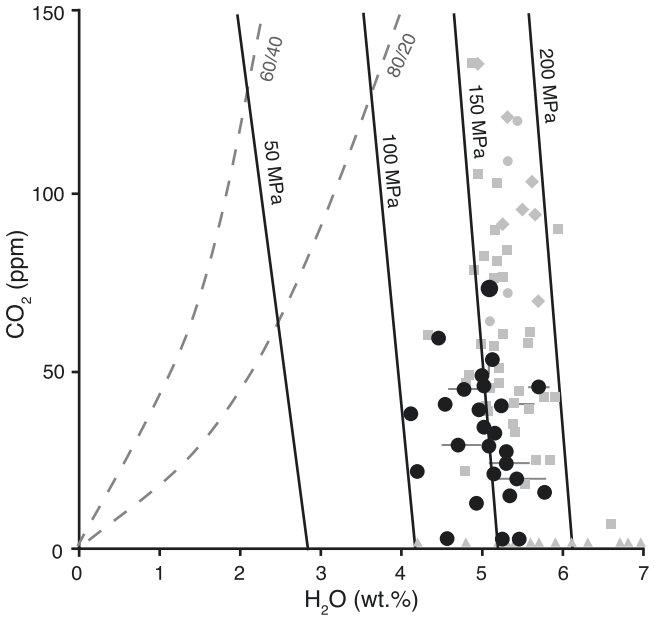

Figure 4. Dissolved volatile contents of early Bishop Tuff glass inclusions (black circles, $n = 28$). Error bars (1σ) are shown in gray when larger than symbol size. Equilibrium solubility at 50, 100, 150, and 200 MPa are shown in black and equilibrium mixed fluid compositions in percent H_2O/CO_2 are shown by dashed gray lines (Liu et al., 2005). Previously published volatile contents from early to middle Bishop Tuff quartz-hosted glass inclusions are shown in gray to demonstrate that our data set is representative (diamonds for Skirius et al. [1990]; triangles for Dunbar and Hervig [1992], who only measured H_2O; squares for Lu et al. [1992]; and circles for Wallace et al. [1999], $n = 68$).

determined by TC/EA. Repeated H^-/O^- measurements on the suite of standards established the nonlinear SIMS calibrations for H_2O in the first and second calibrations (Figures 3 and 7a). Following the calibrations, SIMS analyses indicate the early Bishop Tuff glass inclusions contained 5.2 ± 0.6 wt.% H_2O (1σ), which are indistinguishable from FTIR-derived H_2O contents herein (5.0 ± 0.4 wt.%), and those previously published using both techniques (5.5 ± 0.6 wt.%) (Figure 4 and Table 2) (Dunbar & Hervig, 1992; Lu et al., 1992; Skirius et al., 1990; Wallace et al. 1999).

Although the FTIR and SIMS produce the same overall water content when the inclusions are considered as a group, the correspondence fails when studied on an inclusion-by-inclusion basis. Many inclusions are reproduced within analytical uncertainty; however, other inclusions differ by +0.8 to −2.1 wt.% (e.g., H_2O_{FTIR}-H_2O_{SIMS}) (Table 2). This ambiguity is well displayed when FTIR and SIMS water contents are compared to the hydrogen isotopic compositions of the inclusions (Figure 7). A prominent negative correlation between δD and SIMS-derived H_2O is observed, implying that water-rich inclusions have the most negative δD, with values ranging from −80‰ to −90‰. Conversely, there is no discernable relationship between δD and FTIR-derived water contents.

The incongruous trends displayed by SIMS and FTIR measurements are more likely to be an analytical artifact than a result of natural processes. We acknowledge it is possible that the high-H_2O inclusions (by SIMS) have more negative values of δD resulting from preferential in-diffusion of H as the evolving chamber becomes richer in H_2O. However, this relationship is not observed in H_2O contents measured by FTIR in the same inclusions. Instead, the correlative relationship is more likely caused by a matrix effect during SIMS analyses. Hauri et al. (2006) showed that as the H_2O content of glasses increased, the measured D/H ratio became enriched in H. This outcome was a result of changing sputter yield and H ionization efficiency with increasing H_2O content. These controls on the calculated δD values were most pronounced in Fe-poor rhyolites, like those studied here. The matrix effects generate a decrease of 1‰–5‰ for each increase in wt.% H_2O (Hauri et al., 2006). The D/H ratios enriched in H, as measured here with higher SIMS-derived H_2O content, are thus considered to result from a matrix effect that we could not account for in our calibration. We conclude that the early Bishop Tuff preserves no relationship between δD and H_2O.

Rhyolite glasses with similar H_2O contents and known D/H ratios are needed to confirm the effect of H_2O on the relative yields of the two hydrogen isotopes. Our results suggest that the D/H ratio changes by ~50‰ as H_2O increases by 2.5 wt.%. Support for increasing matrix effects with increasing H_2O content is provided by the curvature in Figures 3a and 3c. A similar H_2O-dependent relationship was observed by Hauri et al. (2002) in basaltic glasses because water impacts the microstructure of silicate glass. In a follow-up study investigating basaltic to rhyolitic glass compositions, Hauri et al. (2006) produced a linear calibration and showed that as the glass H_2O content increases, the ratio of D to H decreases (after normalizing to bulk D/H). The implication for the isotopic composition of the inclusions is that the most trustworthy D/H measurements from our data set are from inclusions containing near 4.2 wt.% H_2O (the H_2O content of the D/H standard closest to glass compositions), with δD value of −40‰ to −60‰.

The difference between FTIR- and SIMS-derived H_2O contents for a specific inclusion cannot be explained by a matrix effect like D/H. Instead, we attribute the differences to the spatial domain analyzed by each technique. FTIR measures a 40 × 40 μm area through the full thickness of the inclusion wafer (30–130 μm, or an analytical volume of ~48,000–208,000 μm^3), whereas SIMS samples a 15-μm-diameter spot that sputters <5 μm depth. Hence, SIMS analyzes a much smaller volume of the inclusion (<1,000 μm^3 and <2% of the FTIR volume), providing a more spatially specific measure of its composition.

Geochemistry, Geophysics, Geosystems

10.1029/2020GC009358

Table 2
Hydrogen Isotopic Composition and Volatile Contents of Quartz-Hosted Rhyolitic Melt Inclusions From the Early Bishop Tuff

	FTIR								SIMS							
Sample	5,200 (abs)	4,500 (abs)	2,350 (abs)	Thickness (μm)	H_2O_m	OH	H_2O (wt.%)	CO_2 (ppm)	D/H	1σ	H (cps)	O (cps)	H^-/O^-	H_2O (wt.%)	δD (‰)	2σ (‰)
1a[a]	0.081	0.029	0.016	113 (2)	3.1	1.1	4.2 (0.1)	22 (1)	1.55E−04	6.60E−07	3.38E+05	1.56E+08	2.17E−03	6.1	−83	9
4[a]	0.071	0.028	0.037	97 (2)	3.2	1.2	4.5 (0.1)	29 (1)	1.54E−04	7.55E−07	3.16E+05	1.39E+08	2.27E−03	6.6	−90	10
10[a]	0.113	0.042	0.011	137 (2)	3.7	1.3	4.9 (0.1)	12 (1)	1.58E−04	3.45E−07	3.38E+05	1.58E+08	2.14E−03	5.9	−66	4
11[a]	0.016	0.006	-	18 (1)	3.9	1.4	5.3 (0.4)	-	1.58E−04	7.95E−07	3.44E+05	1.61E+08	2.13E−03	5.8	−64	10
19	0.031	0.012	0.005	35 (2)	3.9	1.5	5.4 (0.3)	20 (1)	1.74E−04	7.81E−07	2.28E+05	1.34E+08	1.70E−03	4.8	−57	9
22	0.098	0.035	0.034	140 (4)	3.1	1.0	4.1 (0.1)	38 (1)	1.68E−04	3.41E−07	2.45E+05	1.33E+08	1.85E−03	5.7	−89	4
24	0.077	0.029	0.028	97 (3)	3.5	1.2	4.8 (0.2)	45 (2)	1.75E−04	8.26E−07	2.54E+05	1.51E+08	1.68E−03	4.7	−53	9
27	0.078	0.032	0.025	86 (2)	4.1	1.6	5.7 (0.1)	45 (1)	1.73E−04	7.78E−07	2.71E+05	1.55E+08	1.74E−03	5.1	−61	9
30[a]	0.054	0.022	-	73 (2)	3.2	1.3	4.6 (0.1)	-	1.62E−04	3.14E−07	3.10E+05	1.66E+08	1.87E−03	4.5	−42	4
32[a]	0.082	0.032	-	92 (1)	4	1.5	5.4 (0.3)	-	1.58E−04	8.52E−07	2.76E+05	1.43E+08	1.92E−03	4.7	−62	11
33[a]	0.065	0.027	0.012	77 (2)	3.7	1.6	5.3 (0.3)	24 (1)	1.59E−04	7.97E−07	2.73E+05	1.44E+08	1.90E−03	4.6	−61	10
34[a]	0.034	0.012	0.008	42 (3)	3.6	1.1	4.7 (0.3)	29 (2)	1.58E−04	8.25E−07	2.93E+05	1.46E+08	2.01E−03	5.2	−64	10
38b[a]	0.039	0.013	0.012	46 (1)	3.8	1.1	4.9 (0.1)	39 (1)	1.62E−04	3.53E−07	2.48E+05	1.42E+08	1.75E−03	3.9	−43	4
41	0.082	0.031	0.013	96 (2)	3.8	1.3	5.1 (0.1)	21 (1)	1.74E−04	8.04E−07	2.74E+05	1.62E+08	1.69E−03	4.7	−56	9
42	0.081	0.031	0.022	97 (3)	3.7	1.3	5.0 (0.2)	34 (1)	1.70E−04	8.62E−07	3.03E+05	1.68E+08	1.80E−03	5.4	−81	10
44	0.087	0.033	0.026	100 (3)	3.8	1.4	5.2 (0.2)	40 (1)	1.72E−04	2.72E−07	2.75E+05	1.56E+08	1.76E−03	5.2	−68	3
46	0.040	0.014	0.013	51 (1)	3.5	1.1	4.5 (0.1)	40 (1)	1.74E−04	7.06E−07	2.75E+05	1.58E+08	1.74E−03	5.0	−58	8
50_1[b]	0.061	0.027	0.007	74 (2)	3.7	1.7	5.3 (0.2)	14 (1)	1.73E−04	8.82E−07	2.51E+05	1.44E+08	1.74E−03	5.1	−65	10
50_2[b]									1.73E−04	8.43E−07	2.60E+05	1.46E+08	1.78E−03	5.3	−61	10
52b	0.054	0.020	0.021	63 (2)	3.8	1.3	5.1 (0.2)	53 (2)	1.77E−04	1.10E−06	1.68E+05	1.02E+08	1.65E−03	4.5	−41	12
53	0.072	0.030	0.028	90 (2)	3.6	1.4	5.0 (0.1)	48 (1)	1.70E−04	4.40E−07	2.01E+05	1.10E+08	1.82E−03	5.5	−80	5
54_1[b]	0.054	0.020	0.013	63 (2)	3.8	1.4	5.2 (0.1)	32 (1)	1.73E−04	1.14E−06	1.72E+05	9.92E+07	1.74E−03	5.0	−61	13
54_2[b]									1.74E−04	1.02E−06	1.85E+05	1.03E+08	1.79E−03	5.3	−59	12
57	0.085	0.026	0.008	83 (2)	4.6	1.2	5.8 (0.1)	15 (1)	1.68E−04	1.04E−06	1.75E+05	9.38E+07	1.86E−03	5.8	−92	12
60	0.065	0.023	0.020	78 (1)	3.7	1.2	5.0 (0.1)	39 (1)	1.78E−04	7.09E−07	2.45E+05	1.55E+08	1.58E−03	4.2	−37	8
64	0.060	0.022	0.012	68 (3)	3.9	1.3	5.3 (0.2)	27 (1)	1.73E−04	7.50E−07	2.81E+05	1.72E+08	1.64E−03	4.5	−65	9
66	0.040	0.015	0.023	48 (1)	3.7	1.4	5.1 (0.1)	72 (2)	1.70E−04	8.40E−07	2.97E+05	1.58E+08	1.88E-03	5.9	−81	10
68	0.046	0.019	0.010	56 (3)	3.6	1.4	5.1 (0.3)	29 (1)	1.68E−04	7.80E−07	2.87E+05	1.51E+08	1.89E-03	6.0	−87	9
Average (1σ)							**5.0 (0.4)**	**29 (17)**						**5.2 (0.6)**	**−65 (15)**	

Note. FTIR values in parentheses represent 1σ standard deviations. "-" indicates not detected.

Abbreviations: FTIR, Fourier-transform infrared; SIMS, secondary-ion mass spectroscopy.

[a]Analyses in the second calibration. [b] Inclusions 50 and 54 were analyzed twice by SIMS as replicate measurements on neighboring positions in the same inclusion to test reproducibility.

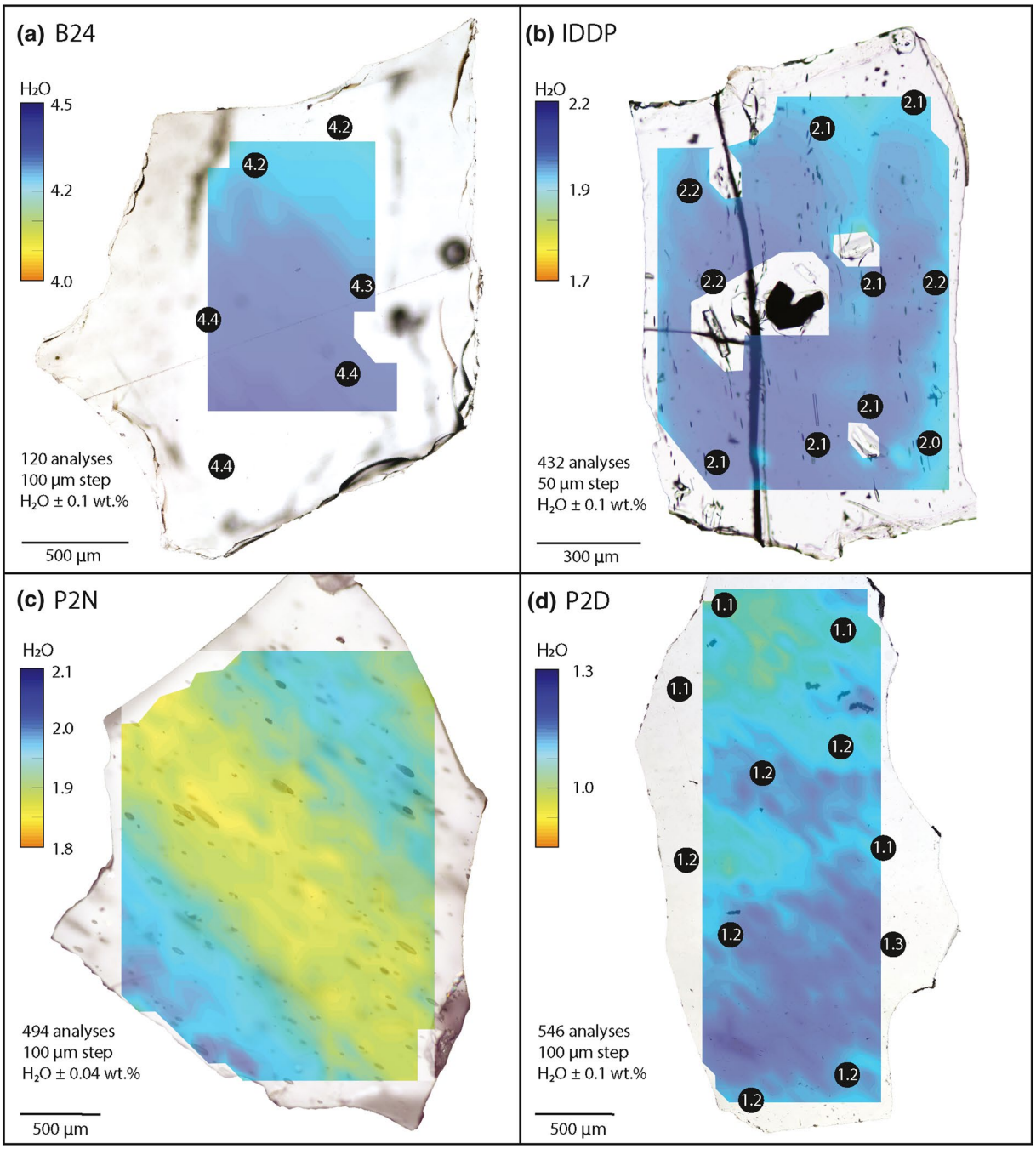

Figure 5. H_2O concentration maps and spot analyses (black circles) overlain on transmitted light photomicrographs of rhyolite reference standards with >1 wt.% H_2O. IDDP, Iceland Deep Drilling Program.

Our analyses demonstrate that early Bishop Tuff inclusions are internally heterogeneous with respect to H_2O content. This result is consistent with other studies. Glass inclusions are known to be compositionally heterogeneous in major and trace elements (e.g., Kent, 2008; Newcombe et al., 2014; Saper & Stolper, 2020). Volatile heterogeneity in glass inclusions has been rarely demonstrated in the literature (e.g., Seaman et al., 2006), but it should be expected. Every glass inclusion study has shown that volatile contents vary from one inclusion to the next. The volatile contents of a magma are estimated using population averages or maximum values. This is the accepted practice even for pristine, glassy materials. Partially crystallized or bubbly inclusions are experimentally rehomogenized to better reflect initial entrapment conditions (e.g.,

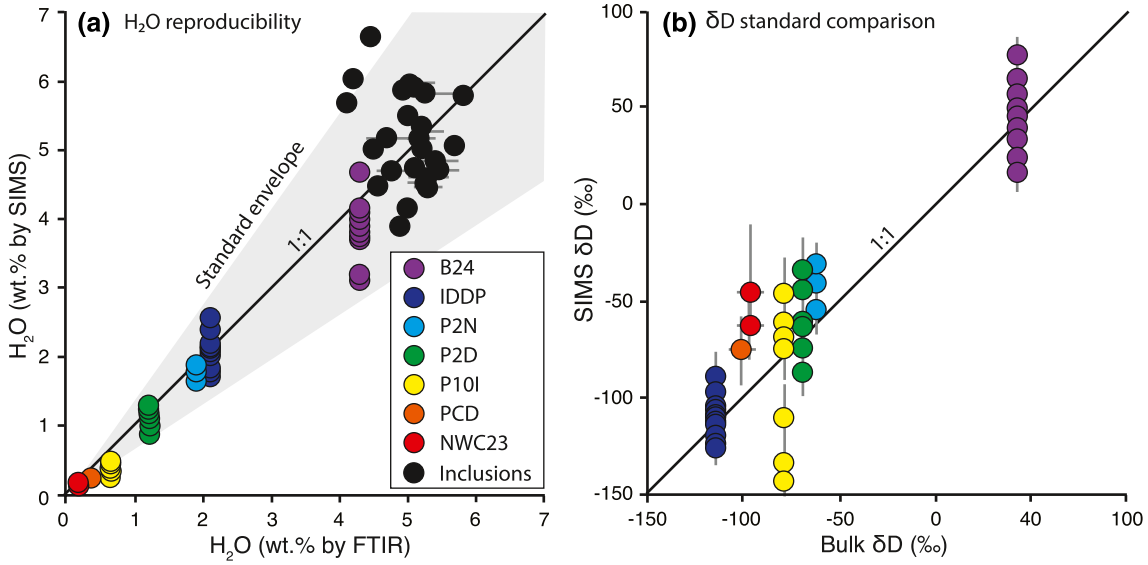

Figure 6. Comparison of the reproducibility of H_2O (a) and hydrogen isotope compositions (b) between secondary-ion mass spectrometry and Fourier-transform infrared measurements of standards and glass inclusions. Error bars are shown in gray when larger than symbol size (δD are 2σ and H_2O are 1σ).

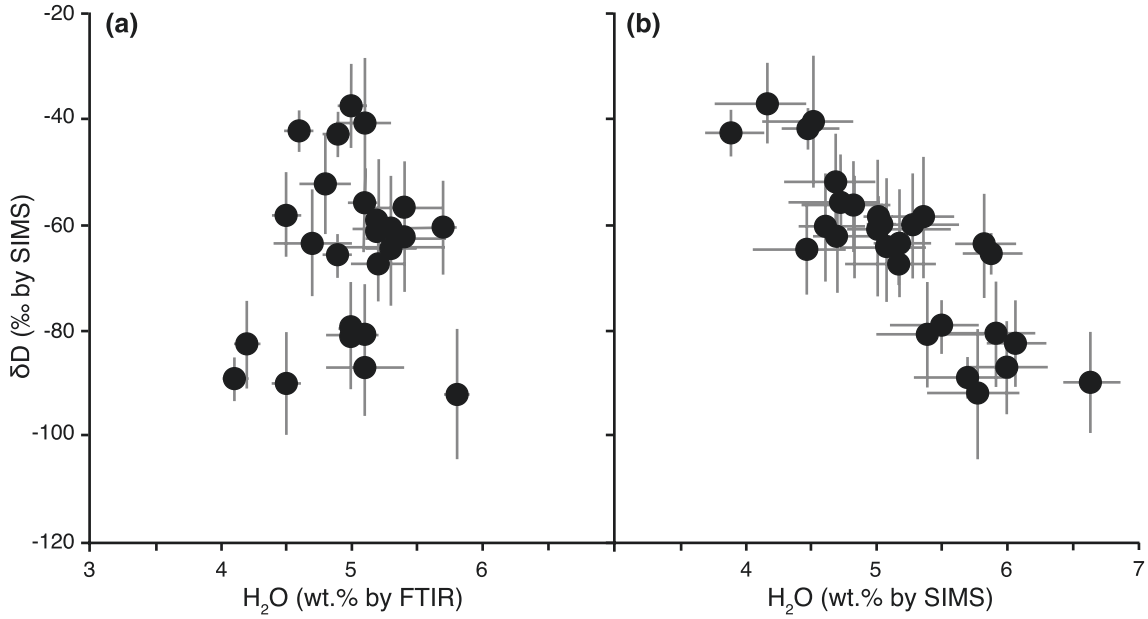

Figure 7. Hydrogen isotope compositions (δD) of early Bishop Tuff rhyolite plotted against (a) H_2O measured by Fourier-transform infrared and (b) secondary-ion mass spectrometry. Error bars are shown in gray when larger than symbol size (δD are 2σ and H_2O are 1σ).

Skirius et al., 1990). The variability within a population is attributed to post-entrapment processes such as crystallization and open- or closed-system degassing (Lowenstern, 1995; Newman & Lowenstern, 2002). Individual inclusions in the early Bishop Tuff may be heterogeneous, even those that appear physically faultless. The internal variability of a single inclusion likely results from the profound structural effects water exerts on melt at the molecular level. Optically homogenous glasses preserve medium-range disorder on scales <100 Å, generating a mixture of water-rich and water-poor domains (Sato et al., 2018; Urakawa et al., 2020). Such structural domains subsequently influence nanolite crystallization and bubble nucleation, which will amplify nano-heterogeneities (e.g., Di Genova et al., 2018; Gonnermann & Gardner, 2013; Mujin & Nakamura, 2014). Water speciation within the inclusion will also change in response to decom-

pression and cooling rates (Wallace et al., 2003; Zhang et al., 1995). We reiterate that SIMS analyses of quickly quenched B24 glass does not display such variability. Thus, the internal variability in the Bishop Tuff glass inclusions is a coarse record of the complex interplay of processes kinetically arrested during ascent, cooling, and transformation of liquid to glass. Building on this observation will likely present rewarding opportunities for future microanalytical studies.

4.2. Causes for Isotopic Fractionation

To further interpret the D/H data, we consider the isotopic fractionation pathways that would be produced by open- and closed-system degassing, diffusive loss, country-rock assimilation, and crystallization.

4.2.1. Open- versus Closed-System Degassing

Energetic degassing of magma drives volcanic eruptions. In many magmatic systems, water is the most abundant volatile. During degassing the ratio of D to H in the residual melt changes toward more negative values as D preferentially partitions to the exsolved vapor. The fractionation follows a speciation-dependent bulk isotopic fractionation factor $\alpha_{\text{vapor-melt}}$. Importantly, α will change as a function of the amount of degassing (F) and the relative abundance of the mole fraction of H_2O and OH^- dissolved in the melt (X_{H2O} and X_{OH}) (Dobson et al., 1989; Newman et al., 1988). We calculate the mole fraction of H_2O and OH^- using the speciation model of VolatileCalc assuming a rhyolite melt degassing from 6 wt.% H_2O at 800°C (Newman & Lowenstern, 2002). The calculation for the bulk vapor-melt fractionation factor is (Rust et al., 2004)

$$\alpha_{vapor-melt} = \left(X_{H2O}\right)_{melt} 10^3 \ln\left(\alpha_{(H2Ovapor-H2Omelt)}\right) + \left(X_{OH}\right)_{melt} 10^3 \ln\left(\alpha_{H2Ovapor-OHmelt}\right) \quad (1)$$

where the fractionation factors for $\alpha_{\text{H2Ovapor-H2Omelt}}$ and $\alpha_{\text{H2Ovapor-OHmelt}}$ are 0.9896 and 1.0415, respectively (after Dobson et al., 1989). Using the bulk value, fractionation during degassing can be modeled using either closed- or open-system assumptions (e.g., Batch and Rayleigh, respectively). Closed-system degassing means the exsolved H_2O vapor stays in equilibrium with the melt:

$$\delta D_{melt} = \delta D_o - [(1 - F) \times \alpha_{vapor-melt}] \quad (2)$$

Closed-system degassing can be visualized as bubbles of exsolved fluid maintaining chemical exchange with melt. Closed-system degassing results in a near-linear decrease in δD with a total isotopic shift of a few tens of ‰ (Figure 8). As permeability increases, H_2O vapor may escape from the system along connected bubble pathways, conduit walls, or fumaroles. This results in open-system degassing, which can be modeled as follows:

$$\delta D_{melt} = \delta D_o - \left[\left(1 - F^{\alpha_{vapor-melt}^{-1}}\right) \times \left(\delta D_o + 1000\right)\right] \quad (3)$$

Open-system degassing results in a pronounced decrease of δD in the residual melt (Figure 8).

Obsidian clasts in pyroclastic air-fall deposits have been shown to contain an array of volatile contents. Those clasts are typically interpreted to represent syn-eruptively quenched parcels of magma, whose individual volatile contents record snapshots of eruptive degassing at variable depths (Castro et al., 2014; Dunbar & Kyle, 1992; Giachetti et al., 2020; Newman et al., 1988; Rust et al., 2004; Taylor et al., 1983). Populations of such clasts from single eruptions typically display open-system Rayleigh degassing trends marked by decreasing D/H values with decreasing H_2O concentrations (e.g., Taylor et al., 1983) (compilation of all published obsidian chips in Figure 8). In some cases, a period of closed-system degassing preludes the open-system degassing signaling a change in the eruptive style from explosive eruption to quiescent dome formation (Newman et al., 1988).

Preeruptive degassing in the Long Valley reservoir must have occurred because the early Bishop Tuff is estimated to have contained significant exsolved gas, equivalent to 5–20 vol.% vapor (Wallace et al., 1995). The

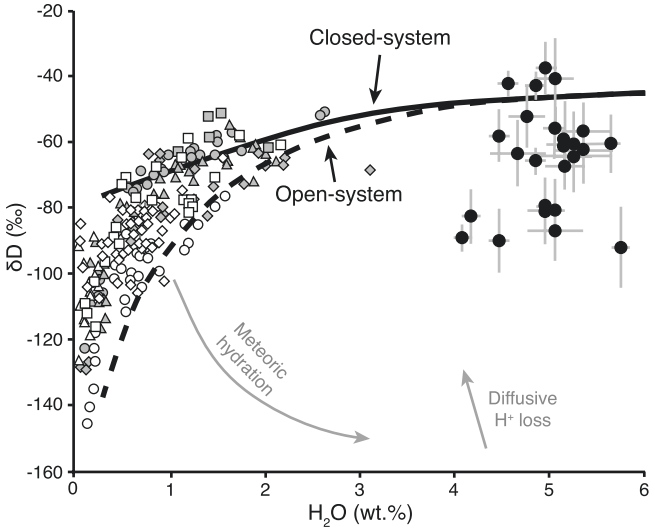

Figure 8. H_2O (Fourier-transform infrared) versus δD (secondary-ion mass spectroscopy) values of early Bishop Tuff glass inclusions (black circles) do not plot along closed- or open-system degassing trends. Error bars are shown in gray when larger than symbol size (δD are 2σ and H_2O are 1σ). Compilation of 176 previously analyzed rhyolitic pyroclastic obsidians are shown in gray and white symbols, gray circles are Mono Craters from Newman et al. (1988); gray triangles are Mono Craters from J. D. Barnes et al. (2014a); gray squares are Mono-Inyo Craters from Taylor et al. (1983); gray diamonds are Medicine Lake from Taylor et al. (1983); white diamonds are Medicine Lake from Giachetti et al. (2020); white circles and triangles are Chaitén and Cordón Caulle, respectively, from Castro et al. (2014); and white squares are Mazama from Mandeville et al. (2009). Uncertainties in those analyses are omitted but are available in the corresponding source. Solid and dashed black lines represent closed-system and open-system degassing models, respectively, assuming an initial magmatic water content of 6 wt.% and −45‰.

style of such degassing was previously unconstrained. Open-system degassing of the reservoir should have produced a systematic isotopic shift of tens of ‰ (Equation 3). Instead, our best estimate for the composition of the early Bishop Tuff is a δD value of −40‰ to −60‰, which projects "upstream" along the trend established by obsidian clasts from pyroclastic air-fall deposits (Figure 8). The absence of an open-system degassing trend in the glass inclusions indicates the reservoir degassed as a closed system. The vapor solely existed as bubbles trapped in a closed reservoir. This suggests that exsolved gases in some magmas may be prevented from escaping to the surface. In such examples, surface fumaroles do not provide direct evidence of subsurface conditions, leaving geodetic measurements of inflation as the only monitoring tool to determine the state of magmatic degassing.

4.2.2. Post-entrapment Diffusive Hydrogen Loss

When molten, melt inclusions become physically isolated from the continually evolving bulk magmatic system. Melt inclusions are far from perfectly closed systems, however. Prior to eruption and quenching at the Earth's surface, inclusions can re-equilibrate with their host crystals and surrounding melt through diffusion. The diffusion of most major and trace element cations is limited by low partitioning behavior and slow diffusion rates in host phases like quartz and olivine. In contrast, hydrogen can diffuse on geologically rapid timescales (e.g., Hauri et al., 2002). Experimental results demonstrate that at magmatic temperatures, olivine-hosted melt inclusions can equilibrate H with the external melt via diffusion in days (e.g., Bucholz et al., 2013; Gaetani et al., 2012), and theoretical calculations suggest quartz-hosted melt inclusions would reach equilibrium with respect to hydrogen in years (e.g., Qin et al., 1992). This post-entrapment diffusive loss causes isotope fractionation, as H protons diffuse more readily than D. Diffusive loss produces inclusions with higher hydrogen isotope ratios. In olivine-hosted glass inclusions, experimental studies and natural samples impacted by post-entrapment H loss display strong negative correlations between δD and H_2O, with >100‰ δD variation in a single suite of glass inclusions from a single sample (Bucholz et al., 2013; Gaetani et al., 2012; Hauri et al., 2002; Walowski et al., 2015).

The early Bishop Tuff glass inclusions does not display strong negative correlations between δD and wt.% H_2O (Figure 8), suggesting that high-temperature diffusive loss is not a primary driver of measured δD variability. Selection of glassy inclusions from a pyroclastic fall deposit suggests geologically rapid quenching occurred in our samples, and thus, reduces the likelihood of diffusive H loss (Lloyd et al., 2013). Further, there is no relationship between D/H and inclusion size, position relative to crystal faces, or water speciation, suggesting negligible low-temperature diffusive loss of H_2O_m that would not fractionate D from H (Hudak & Bindeman, 2020).

4.2.3. Meteoric Rehydration

Meteoric waters infiltrate and modify the composition of volcanic glass following eruptive emplacement on timescales of <10–10^4 years (Cassel & Breeker, 2017; Giachetti et al., 2020; Nolan & Bindeman, 2013; Seligman et al., 2018). The meteoric water modifies the primary magmatic hydrogen isotope composition initially preserved in volcanic glass because meteoric waters are enriched in D relative to H, with the ratio controlled by precipitation, temperature, latitude, and altitude (e.g., Cassel et al., 2009; Giachetti et al., 2020, 2015; Hudak & Bindeman, 2018; Ingraham & Taylor, 1991; Jackson et al., 2019; Seligman et al., 2016). Meteoric water and groundwater in the vicinity of Long Valley have δD in the range of −90‰ to −110‰,

values enriched in H relative to D as expected on the rain shadowed, high-altitude eastern flank of the Sierra Nevada (Friedman et al., 2002; Ingraham & Taylor, 1991). Indeed, rehydrated Bishop Tuff glass has very low δD value of −134‰ (Mulch et al., 2008).

The rhyolitic glass inclusions are fully encased within a protective crystalline quartz vessel, which were each extracted from rapidly quenched pumices. Diffusive rehydration would initially enrich H over the relatively slower D, thus producing more negative δD with increasing wt.% H_2O (e.g., Seligman et al., 2016). However, over longer time periods, the D would also have sufficient time to diffuse, thus reducing fractionation. The ~760 ka since eruption of the Bishop Tuff certainly presents a long timescale for diffusion. Total H_2O contents appear unmodified. In addition, the diffusive exchange of hydrogen is very slow in quartz at ambient conditions, $<10^{-17.5}$ $m^2 \cdot s^{-1}$, although better calibrations for both D and H await future experimental constraints (e.g., Biró et al., 2017). Nevertheless, the inclusion data do not plot along a rehydration evolution trend (Figure 8). Nor does δD correlate with the position of the inclusion within the quartz host. We conclude that it is unlikely that the hydrogen isotope compositions of the glassy inclusions were modified by rehydration.

4.2.4. Assimilation and Fractional Crystallization

Despite debate regarding the preeruptive storage and evolution of the Bishop Tuff reservoir (e.g., Chamberlain et al., 2015; Evans et al., 2016; Gardner et al., 2014; Gualda & Ghiorso, 2013), mineralogically and geochemically differences are evident between the early and late Bishop Tuff (e.g., Hildreth & Wilson, 2007). The early Bishop Tuff fall deposit studied here is a high-silica rhyolite with a mineral assemblage dominated by quartz, sanidine, and plagioclase (3:3:1 ratio, respectively, Hildreth, 1979), with minor amounts of biotite and magnetite, and no pyroxene (which is present in all late-erupted units). Most mineralogical arguments using those phases agree that the early- and late-erupted materials did not interact (e.g., Gualda & Ghiorso, 2013; Hildreth & Wilson, 2007), and that late-erupted materials alone show evidence for a recharge event that may have triggered eruption (Evans & Bachmann, 2013, and references therein).

The isotopic composition of the reservoir was not affected by anhydrous mineral phases. The presence of a hydrous phase, biotite, necessitates consideration of δD fractionation during crystallization. At magmatic temperatures, crystallization of biotite is likely to drive residual melt to more positive δD (biotite → H_2O, $1{,}000 \ln \alpha_{\text{biotite-H2O}} = -25.3$ @ $T = 700$°C, Suzuoki & Epstein, 1976). Biotite is found in small concentrations in the early Bishop Tuff (<4% of the phenocryst population, which itself is <5% of the bulk, Hildreth, 1979). It is unlikely to have changed δD values by more than a few ‰, less than the measured analytical uncertainty. Interestingly, Gualda (2007) suggested that the millimeter-scale melt heterogeneity that may have produced the bright cathodoluminescence (CL) quartz rims could be explained by decompression-driven biotite breakdown. Although local (millimeter-scale) variability in biotite stability could drive variability in δD values, the location of analyzed inclusions in crystal interiors, far from the bright CL rims, rules out this process.

Another important consideration for measured δD compositions is the impact of assimilation processes that commonly occur in the crustal reservoirs. Although some previous work suggests that assimilation of crustal material did not play a role in contributing to the compositional variability observed between the early- and late-erupted units of the Bishop Tuff (e.g., Hildreth & Wilson, 2007), contamination of the magma by surrounding country rock is likely to be significant during the assembly of any large-volume magmatic system in the upper crust. Here, the contributions are wall rocks of Mesozoic Sierran granitoids and reservoir roof of Paleozoic marine shales (Hildreth et al., 2018). Masi et al. (1981) found that Sierran granitoids display a large range in δD (−131‰ to −46‰), whereas shales typically have δD between −60‰ and −100‰ (Bindeman et al., 2016). Assimilation of these materials would lead to a magmatic composition with unchanged or isotopically lighter hydrogen.

Previous investigations of other stable isotope systems and radiogenic isotopes can provide additional insight into the role of assimilation. The surrounding country rocks have distinctly radiogenic isotope compositions, but perhaps surprisingly, Sr isotope studies find little evidence for significant crustal assimilation in the early Bishop Tuff (Halliday et al., 1984; Knesel & Davidson, 1997). Oxygen isotope studies demonstrate higher $\delta^{18}O$ values than the mantle, indicative of fractionation and assimilation of a crustal component. However, oxygen

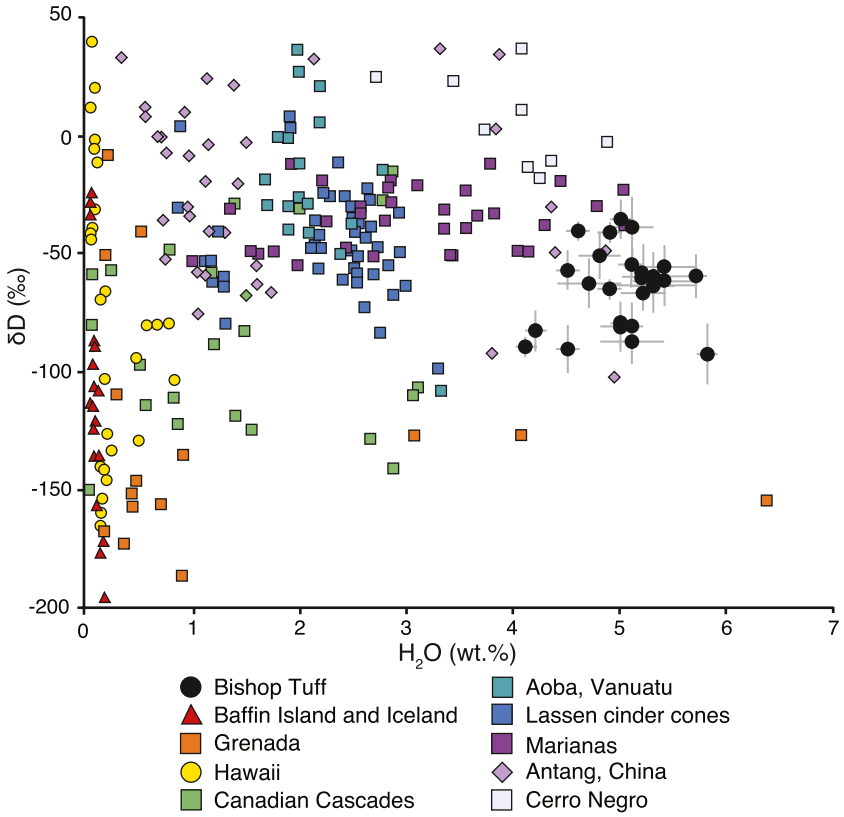

Figure 9. Comparison of the hydrogen isotopic composition of Bishop Tuff rhyolitic glass inclusions (black circles) with a global compilation of all previous analyses in basaltic glass inclusions, which have been restricted entirely to mafic compositions ($n = 240$). Error bars are shown in gray when larger than symbol size (δD are 2σ and H_2O are 1σ). Uncertainties in earlier analyses are omitted but are available in the corresponding source. Symbols are used to differentiate tectonic setting, and squares are used to show arc-related magmas. Hawaiian basalts from Hauri (2002), Baffin Island and Iceland picrites from Hallis et al. (2015), Canadian Cascade basalts from Venugopal et al. (2020), Grenada basalt from Bouvier et al. (2010), Antang, China, basalts from Wu et al. (2020, p. 105337), Aoba, Vanuatu alkali basalts from Métrich and Deloule (2014), Marianas arc units from Shaw et al. (2008), Lassen cinder cones from Walowski et al. (2015), and Cerro Negro basalt from Bucholz et al. (2013) and Gaetani et al. (2012).

isotopes rule out assimilation of materials hydrothermally altered by meteoric H_2O, which would drive melts to compositions more enriched in H relative to D (Bindeman & Valley, 2002).

Taken together, fractionation and assimilation processes that occurred during the storage and evolution of the early Bishop Tuff could result in both positive and negative excursions in δD from initial mantle values. However, the previous mineralogical and isotopic investigations outlined above suggest that the impacts of differentiation are unlikely to have an impact on δD greater than the uncertainty and measured spread in our data set, such that the presented hydrogen isotope compositions likely represent estimates of the initial δD of the mantle-derived melts from which the rhyolitic magmas evolved.

4.3. Petrogenesis and Mantle Source Compositions

Long Valley Caldera is not located in a tectonic regime traditionally associated with abundant magmatism (e.g., a hotspot or subduction zone). The complexity of tectonics in California throughout the past 30 Ma has led to numerous hypotheses related to the generation of magma in the Sierra Nevada and Walker Lane in the Cenozoic (Putirka et al., 2012). Various studies have concluded that initiation of the San Andreas Fault system, migration of the Mendocino Triple Junction, and sinking of the remnant Farallon slab have contributed to asthenospheric upwelling and lithospheric degradation beneath the Sierra Nevada (Putirka et al., 2012, and references therein).

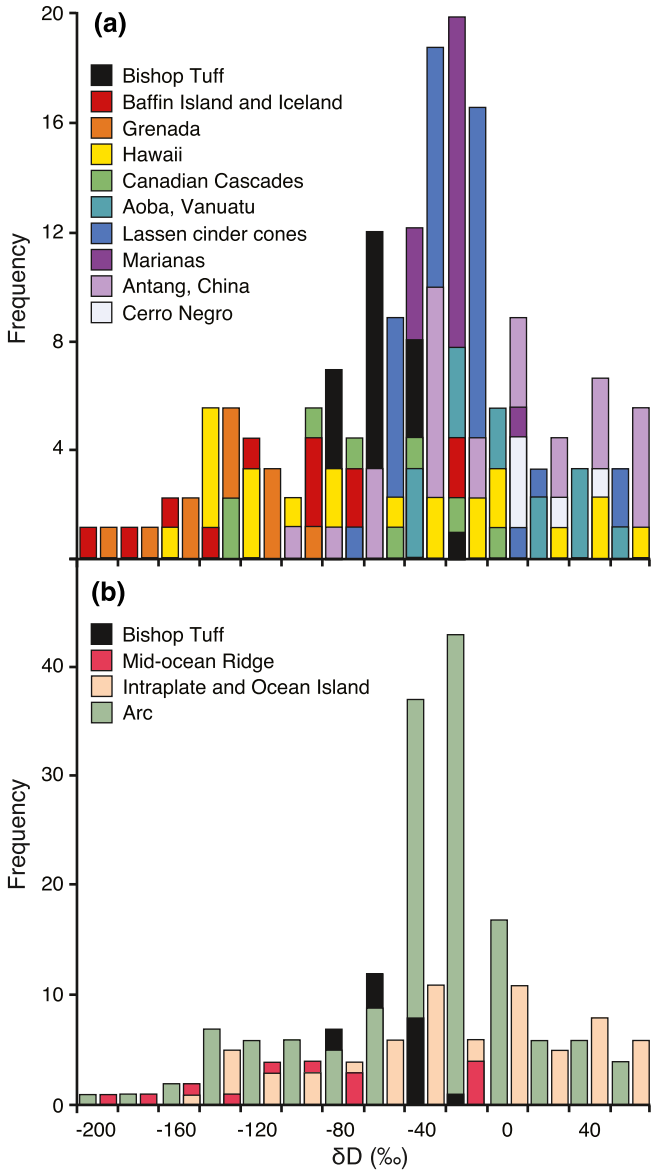

Figure 10. Hydrogen isotopic composition of rhyolitic early Bishop Tuff glass inclusions compared to basaltic inclusions from different (a) volcanic systems and (b) tectonic environments. Same color scheme and references as Figure 9. Hawaiian basalts from Hauri (2002), Baffin Island and Iceland picrites from Hallis et al. (2015), Canadian Cascade basalts from Venugopal et al. (2020), Grenada basalt from Bouvier et al. (2010), Antang, China, basalts from Wu et al. (2020, p. 105337), Aoba and Vanuatu alkali basalts from Métrich and Deloule (2014), Marianas arc units from Shaw et al. (2008), Lassen cinder cones from Walowski et al. (2015), and Cerro Negro basalt from Bucholz et al. (2013) and Gaetani et al. (2012).

The petrogenesis of the large-volume Bishop Tuff reservoir thus remains a key question. The answer is inherently tied to mantle process, which may be informed by our D/H measurements. The hydrogen isotope composition of the mantle is heterogeneous and varies globally. Variability is controlled by plate tectonic environment and mantle dynamics. Analyses of glassy MORB suggest that the δD of the mantle source varies with degree of enrichment (e.g., mantle reservoirs like DMM, HIMU, EM1, and EM2) and geography, with recent estimates of δD ranging from −40‰ to −100‰ (Dixon et al., 2017, and references therein). Typical arc basalts display more positive δD than MORB. Arc basalts δD values regularly range from −10‰ to −60‰ because the mantle may be metasomatized by D-enriched slab fluids (Dixon et al., 2017; Giggenbach, 1992; Shaw et al., 2008; Walowski et al., 2015). Mantle reservoirs sampled by ocean island basalts are also diverse and have δD values that vary significantly (Figures 9 and 10) (e.g., Dixon et al., 2017; Kyser & O'Neil, 1984; Kingsley et al., 2002; Loewen et al., 2019).

Hotspot magmatism that impinges upon overriding continental crust is further complicated by assimilation and fractional crystallization. The Yellowstone hot spot is thought to have an initial magmatic δD in the range of −70‰ to −90‰ based on D/H in amphibole from the Lava Creek Tuff (Loewen & Bindeman, 2015; Martin et al., 2017). Because Long Valley Caldera shares some aspects with Yellowstone, the Bishop Tuff has been inferred to have a δD value of −80‰ to −90‰ (Martin et al., 2017). Important similarities that may generate or modify the isotopic composition of magmas do exist between these caldera systems, including the formation of a large-volume, rhyolitic reservoir by fractional crystallization of basaltic melts and assimilation within a 40- to 50-km-thick crustal filter (Chulick & Mooney, 2002; Hill, 1976; Metz & Mahood, 1991; Yuan et al., 2010). Differences also exist. Radiogenic isotope studies of Bishop Tuff magmas suggest evolution by extensive fractional crystallization of basaltic magmas derived from an enriched lithospheric mantle source (Cousens, 1996; Knesel & Davidson, 1997), whereas Yellowstone magmas are plume derived. At Long Valley, trace element enrichments in regional mantle-derived melts are thought to have been imparted to the lithosphere by dehydration of the Laramide-age Farallon slab. The hydrogen isotope composition of the Bishop Tuff presents evidence for such a persistent slab signature (e.g., characterized by δD relatively enriched in D), suggesting petrologic modifications contributed by the Farallon slab are present in the rhyolite. No estimates exist for the hydrogen isotopic composition of the mantle in the Sierra Nevada/Basin and Range region of western North America.

To further explore the significance of the hydrogen isotope composition of the Bishop Tuff glass inclusions, we compare our measurements to a global, terrestrial data set of δD measured specifically in basaltic glass inclusions (Figures 9 and 10). To date, no studies have explored more silicic compositions. Despite higher water contents, we find that the early Bishop Tuff inclusions are most similar to a compilation of arc magmas, including those from the southern Cascades (Walowski et al., 2016). δD in early Bishop Tuff inclusions is consistent with interpretations of an enriched mantle source with modifications contributed by the Farallon slab, as has been suggested for regional quaternary Sierra Nevada and Walker Lane basaltic magmas (Putirka et al., 2012).

5. Conclusion

Quartz-hosted, rhyolitic glass inclusions from the early Bishop Tuff display a range of δD, spanning from −38‰ to −92‰. The most negative values arise from analytical effects. δD values ranging from −40‰ to −60‰ are considered to be the most representative of the early Bishop Tuff magma reservoir. Comparisons between FTIR- and SIMS-derived wt.% H_2O indicate the glass inclusions are internally heterogeneous with respect to water content. Such heterogeneity is attributed to structural changes during quenching. Glass inclusions preserve no systematic decrease in δD values with decreasing water contents, as would be expected with open-system degassing processes in the reservoir. This suggests that the Long Valley reservoir behaved as a closed system and exsolved gases remained trapped in the reservoir as bubbles. There was negligible degassing of volatiles to the surface, which may inform modern monitoring efforts of fumarolic systems at Long Valley and elsewhere. There is a similar lack of evidence for isotopic fractionation by rehydration, fractional crystallization, or assimilation. The D/H values of early Bishop Tuff glass inclusions thus represent an isolated isotopic reservoir. Through a comparison with a global compilation δD measured in basaltic glass inclusions, our results support a subduction-related source, perhaps modified by contributions from the Farallon slab.

Data Availability Statement

Data is archived in the EarthChem data repository at https://doi.org/10.26022/IEDA/111731. Datasets compiled for use in this paper are available in the in-text references and are summarized here: Pyroclastic obsidians are from J. D Barnes et al. (2014a), Castro et al. (2014), Giachetti et al. (2020), Mandeville et al. (2009), Newman et al. (1988), and Taylor et al. (1983); Basaltic melt inclusions are from Bouvier et al. (2010), Bucholz et al. (2013), Gaetani et al. (2012), Hallis et al. (2015), Hauri (2002), Métrich and Deloule (2014), Shaw et al. (2008), Venugopal et al. (2020), Walowski et al. (2015), and Wu et al. (2020, p. 105337).

Acknowledgments
The authors declare no competing financial interests. We thank J. D. Barnes, C. Bucholz, L. Jackson, and I. Bindeman for careful reviews. J. D. Barnes and T. Larsen provided D/H water standards. We acknowledge the use of the Arizona State University SIMS Facility supported by a grant from the US National Science Foundation (EAR-1819550). This study was also partially supported by EAR-1725003 to Kenneth S. Befus.

References

Anderson Jr, A. T., Newman, S., Williams, S. N., Druitt, T. H., Skirius, C., & Stolper, E. (1989). H_2O, CO_2, CI, and gas in Plinian and ash-flow Bishop rhyolite. *Geology*, *17*(3), 221–225.

Barnes, J. D., Prather, T. J., Cisneros, M., Befus, S. K., Gardner, J. E., & Larson, T. E. (2014a). Stable chlorine isotope behavior during volcanic degassing of H_2O and CO_2 at Mono Craters, CA. *Bulletin of Volcanology*, *76*, 805.

Barnes, J. J., Tartèse, R., Anand, M., McCubbin, F. M., Franchi, I. A., Starkey, N. A., & Russell, S. S. (2014b). The origin of water in the primitive Moon as revealed by the lunar highlands samples. *Earth and Planetary Science Letters*, *390*, 244–252.

Behrens, H., Tamic, N., & Holtz, F. (2004). Determination of the molar absorption coefficient for the infrared absorption band of CO_2 in rhyolitic glasses. *American Mineralogist*, *89*, 301–306.

Bindeman, I. N., Bekker, A., & Zakharov, D. O. (2016). Oxygen isotope perspective on crustal evolution on early Earth: A record of Precambrian shales with emphasis on Paleoproterozoic glaciations and Great Oxygenation Event. *Earth and Planetary Science Letters*, *437*, 101–113.

Bindeman, I. N., & Valley, J. W. (2002). Oxygen isotope study of the Long Valley magma system, California: Isotope thermometry and convection in large silicic magma bodies. *Contributions to Mineralogy and Petrology*, *144*, 185–205.

Biró, T., Kovács, I. J., Karátson, D., Stalder, R., Király, E., Falus, G., & Sándorné, J. K. (2017). Evidence for post-depositional diffusional loss of hydrogen in quartz phenocryst fragments within ignimbrites. *American Mineralogist*, *102*, 1187–1201.

Blundy, J., & Cashman, K. (2005). Rapid decompression-driven crystallization recorded by melt inclusions from Mount St. Helens volcano. *Geology*, *33*, 793–796.

Bouvier, A. S., Métrich, N., & Deloule, E. (2010). Light elements, volatiles, and stable isotopes in basaltic melt inclusions from Grenada, Lesser Antilles: Inferences for magma genesis. *Geochemistry, Geophysics, Geosystems*, *11*(9), 1–20. https://doi.org/10.1029/2010GC003051

Bucholz, C. E., Gaetani, G. A., Behn, M. D., & Shimizu, N. (2013). Post-entrapment modification of volatiles and oxygen fugacity in olivine-hosted melt inclusions. *Earth and Planetary Science Letters*, *374*, 145–155.

Cassel, E. J., & Breecker, D. O. (2017). Long-term stability of hydrogen isotope ratios in hydrated volcanic glass. *Geochimica et Cosmochimica Acta*, *200*, 67–86. https://doi.org/10.1016/j.gca.2016.12.001

Cassel, E. J., Graham, S. A., & Chamberlain, C. P. (2009). Cenozoic tectonic and topographic evolution of the northern Sierra Nevada, California, through stable isotope paleoaltimetry in volcanic glass. *Geology*, *37*, 547–550.

Cassel, E. J., Graham, S. A., Chamberlain, C., & Henry, C. D. (2012). Early Cenozoic topography, morphology, and tectonics of the northern Sierra Nevada and western Basin and Range. *Geosphere*, *8*, 229–249.

Castro, J. M., Bindeman, I. N., Tuffen, H., & Schipper, C. I. (2014). Explosive origin of silicic lava: Textural and δD–H_2O evidence for pyroclastic degassing during rhyolite effusion. *Earth and Planetary Science Letters*, *405*, 52–61.

Chamberlain, K. J., Wilson, C. J., Wallace, P. J., & Millet, M. A. (2015). Micro-analytical perspectives on the Bishop Tuff and its magma chamber. *Journal of Petrology*, *56*, 605–640.

Chen, J. F., Schauer, S., & Hervig, R. (2013). NEG alignment method for negative ion analysis on insulators by magnetic sector SIMS. *Nuclear Instruments and Methods in Physics Research B*, *295*, 50–54.

Chulick, G. S., & Mooney, W. D. (2002). Seismic structure of the crust and uppermost mantle of North America and adjacent oceanic basins: A synthesis. *Bulletin of the Seismological Society of America*, *92*, 2478–2492.
Cousens, B. L. (1996). Magmatic evolution of Quaternary mafic magmas at Long Valley Caldera and the Devils Postpile, California: Effects of crustal contamination on lithospheric mantle-derived magmas. *Journal of Geophysical Research*, *101*, 27673–27689.
Di Genova, D., & Caracciolo, A., & Kolzenburg, S. (2018). Measuring the degree of "nanotilization" of volcanic glasses: Understanding syn-eruptive processes recorded in melt inclusions. *Lithos*, *318*, 209–218.
Dixon, J. E., Bindeman, I. N., Kingsley, R. H., Simons, K. K., Le Roux, P. J., & Hajewski, T. R. (2017). Light stable isotopic compositions of enriched mantle sources: Resolving the dehydration paradox. *Geochemistry, Geophysics, Geosystems*, *18*(11), 3801–3839.
Dobson, P. F., Epstein, S., & Stolper, E. M. (1989). Hydrogen isotope fractionation between coexisting vapor and silicate glasses and melts at low pressure. *Geochimica et Cosmochimica Acta*, *53*, 2723–2730.
Dunbar, N. W., & Hervig, R. L. (1992). Petrogenesis and volatile stratigraphy of the Bishop Tuff: Evidence from melt inclusion analysis. *Journal of Geophysical Research*, *97*, 15129–15150.
Dunbar, N. W., & Kyle, P. R. (1992). Volatile contents of obsidian clasts in tephra from the Taupo Volcanic Zone, New Zealand: Implications to eruptive processes. *Journal of Volcanology and Geothermal Research*, *49*, 127–145.
Evans, B. W., & Bachmann, O. (2013). Implications of equilibrium and disequilibrium among crystal phases in the Bishop Tuff. *American Mineralogist*, *98*, 274–274.
Evans, B. W., Hildreth, W., Bachmann, O., & Scaillet, B. (2016). In defense of magnetite-ilmenite thermometry in the Bishop Tuff and its implication for gradients in silicic magma reservoirs. *American Mineralogist*, *101*, 469–482.
Friedman, I., Smith, G. I., Johnson, C. A., & Moscati, R. J. (2002). Stable isotope compositions of waters in the Great Basin, United States 2. Modern precipitation. *Journal of Geophysical Research*, *107*, 1–15. https://doi.org/10.1029/2001JD000566
Gaetani, G. A., O'Leary, J. A., Shimizu, N., Bucholz, C. E., & Newville, M. (2012). Rapid reequilibration of H_2O and oxygen fugacity in olivine-hosted melt inclusions. *Geology*, *40*, 915–918.
Gaetani, G. A., & Watson, E. B. (2002). Modeling the major-element evolution of olivine-hosted melt inclusions. *Chemical Geology*, *183*, 25–41.
Gardner, J. E., Befus, K. S., Gualda, G. A., & Ghiorso, M. S. (2014). Experimental constraints on rhyolite-MELTS and the Late Bishop Tuff magma body. *Contributions to Mineralogy and Petrology*, *168*, 1051.
Giachetti, T., Gonnermann, H. M., Gardner, J. E., Shea, T., & Gouldstone, A. (2015). Discriminating secondary from magmatic water in rhyolitic matrix-glass of volcanic pyroclasts using thermogravimetric analysis. *Geochimica et Cosmochimica Acta*, *148*, 457–476. https://doi.org/10.1016/j.gca.2014.10.017
Giachetti, T., Hudak, M. R., Shea, T., Bindeman, I. N., & Hoxsie, E. C. (2020). D/H ratios and H_2O contents record degassing and rehydration history of rhyolitic magma and pyroclasts. *Earth and Planetary Science Letters*, *530*, 115909.
Giggenbach, W. F. (1992). Isotopic shifts in waters from geothermal and volcanic systems along convergent plate boundaries and their origin. *Earth and Planetary Science Letters*, *113*(4), 495–510.
Gonnermann, H. M., & Gardner, J. E. (2013). Homogeneous bubble nucleation in rhyolitic melt: Experiments and nonclassical theory. *Geochemistry, Geophysics, Geosystems*, *14*, 4758–4773. https://doi.org/10.1002/ggge.20281
Gualda, G. A. (2007). *Crystal and bubble populations in the early-erupted Bishop rhyolitic magma: Microscopy, X-ray tomography and microanalysis of pumice clasts*, (–). Chicago, IL: . The University of Chicago.
Gualda, G. A., & Ghiorso, M. S. (2013). The Bishop Tuff giant magma body: An alternative to the standard model. *Contributions to Mineralogy and Petrology*, *166*, 755–775.
Halliday, A. N., Fallick, A. E., Hutchinson, J., & Hildreth, W. (1984). A Nd, Sr and O isotopic investigation into the causes of chemical and isotopic zonation in the Bishop Tuff, California. *Earth and Planetary Science Letters*, *68*, 379–391.
Hallis, L. J., Huss, G. R., Nagashima, K., Taylor, G. J., Halldórsson, S. A., Hilton, D. R., & Meech, K. J. (2015). Evidence for primordial water in Earth's deep mantle. *Science*, *350*, 795–797.
Hauri, E. (2002). SIMS analysis of volatiles in silicate glasses, 2: Isotopes and abundances in Hawaiian melt inclusions. *Chemical Geology*, *183*, 115–141.
Hauri, E., Wang, J., Dixon, J. E., King, P. L., Mandeville, C., & Newman, S. (2006). SIMS analysis of volatiles in silicate glasses: 1. Calibration, matrix effects and comparisons with FTIR. *Chemical Geology*, *183*, 99–114.
Hildreth, W. (1979). The Bishop Tuff: Evidence for the origin of compositional zonation in silicic magma chambers. *Geological Society of America Special Paper*, *180*, 43–75.
Hildreth, W., & Wilson, C. J. (2007). Compositional zoning of the Bishop Tuff. *Journal of Petrology*, *48*(5), 951–999.
Hildreth, W., Ryan-Davis, J., & Harlow, B. (2018). Graphite in the Bishop Tuff and its effect on postcaldera oxygen fugacity. *Geosphere*, *14*(1), 343–359.
Hill, D. P. (1976). Structure of Long Valley Caldera, California, from a seismic refraction experiment. *Journal of Geophysical Research*, *81*, 745–753.
Hudak, M. R., & Bindeman, I. N. (2018). Conditions of pinnacle formation and glass hydration in cooling ignimbrite sheets from H and O isotope systematics at Crater Lake and the Valley of Ten Thousand Smokes. *Earth and Planetary Science Letters*, *500*, 56–66.
Hudak, M. R., & Bindeman, I. N. (2020). Solubility, diffusivity, and O isotope systematics of H_2O in rhyolitic glass in hydrothermal temperature experiments. *Geochimica et Cosmochimica Acta*, *283*, 222–242. https://doi.org/10.1016/j.gca.2020.06.009
Ingraham, N. L., & Taylor, B. E. (1991). Light stable isotope systematics of large-scale hydrologic regimes in California and Nevada. *Water Research*, *27*, 77–90.
Jackson, L. J., Horton, B. K., Beate, B. O., Bright, J., & Breecker, D. O. (2019). Testing stable isotope paleoaltimitry with Quaternary volcanic glasses from the Ecuadorian Andes. *Geology*, *47*, 411–414.
Johnson, E. R., Wallace, P. J., Cashman, K. V., Granados, H. D., & Kent, A. J. (2008). Magmatic volatile contents and degassing-induced crystallization at Volcán Jorullo, Mexico: Implications for melt evolution and the plumbing systems of monogenetic volcanoes. *Earth and Planetary Science Letters*, *269*, 478–487.
Kent, A. J. (2008). Melt inclusions in basaltic and related volcanic rocks. *Reviews in Mineralogy and Geochemistry*, *69*, 273–331.
Kingsley, R. H., Schilling, J. G., Dixon, J. E., Swart, P., Poreda, R., & Simons, K. (2002). D/H ratios in basalt glasses from the Salas y Gomez mantle plume interacting with the East Pacific Rise: Water from old D-rich recycled crust or primordial water from the lower mantle? *Geochemistry, Geophysics, Geosystems*, *3*, 1–26. https://doi.org/10.1029/2001GC000199
Knesel, K. M., & Davidson, J. P. (1997). The origin and evolution of large-volume silicic magma systems: Long Valley caldera. *International Geology Review*, *39*, 1033–1052.
Kyser, T. K., & O'Neil, J. R. (1984). Hydrogen isotope systematics of submarine basalts. *Geochimica et Cosmochimica Acta*, *48*, 2123–2133.

Liu, Y., Zhang, Y., & Behrens, H. (2005). Solubility of H_2O in rhyolitic melts at low pressures and a new empirical model for mixed H_2O–CO_2 solubility in rhyolitic melts. *Journal of Volcanology and Geothermal Research*, *143*, 219–235. https://doi.org/10.1016/j.jvolgeores.2004.09.019

Lloyd, A. S., Plank, T., Ruprecht, P., Hauri, E. H., & Rose, W. (2013). Volatile loss from melt inclusions in pyroclasts of differing sizes. *Contributions to Mineralogy and Petrology*, *165*, 129–153.

Loewen, M. W., & Bindeman, I. N. (2015). Oxygen isotope and trace element evidence for three-stage petrogenesis of the youngest episode (260-79 ka) of Yellowstone rhyolitic volcanism. *Contributions to Mineralogy and Petrology*, *170*, 39.

Loewen, M. W., Graham, D. W., Bindeman, I. N., Lupton, J. E., & Garcia, M. O. (2019). Hydrogen isotopes in high 3He/4He submarine basalts: Primordial vs. recycled water and the veil of mantle enrichment. *Earth and Planetary Science Letters*, *508*, 62–73.

Lowenstern, J. B. (1995). Applications of silicate-melt inclusions to the study of magmatic volatiles. *Magmas, Fluids and Ore Deposits*, *23*, 71–99.

Lu, F., Anderson, A. T., & Davis, A. M. (1992). Melt inclusions and crystal-liquid separation in rhyolitic magma of the Bishop Tuff. *Contributions to Mineralogy and Petrology*, *110*, 113–120.

Mandeville, C. W., Webster, J. D., Tappen, C., Taylor, B. E., Timbal, A., Sasaki, A., & Bacon, C. R. (2009). Stable isotope and petrologic evidence for open-system degassing during the climactic and pre-climactic eruptions of Mt. Mazama, Crater Lake, Oregon. *Geochimica et Cosmochimica Acta*, *73*, 2978–3012. https://doi.org/10.1016/j.gca.2009.01.019

Martin, E., Bindeman, I., Balan, E., Palandri, J., Seligman, A., & Villemant, B. (2017). Hydrogen isotope determination by TC/EA technique in application to volcanic glass as a window into secondary hydration. *Journal of Volcanology and Geothermal Research*, *348*, 49–61. https://doi.org/10.1016/j.jvolgeores.2017.10.013

Masi, U., O'Neil, J. R., & Kistler, R. W. (1981). Stable isotope systematics in Mesozoic granites of central and northern California and southwestern Oregon. *Contributions to Mineralogy and Petrology*, *76*(1), 116–126.

Métrich, N., & Deloule, E. (2014). Water content, δD and δ11B tracking in the Vanuatu arc magmas (Aoba Island): Insights from olivine-hosted melt inclusions. *Lithos*, *206*, 400–408.

Metz, J. M., & Mahood, G. A. (1991). Development of the Long Valley, California, magma chamber recorded in precaldera rhyolite lavas of Glass Mountain. *Contributions to Mineralogy and Petrology*, *106*, 379–397.

Mujin, M., & Nakamura, M. (2014). A nanolite record of eruption style transition. *Geology*, *42*, 611–614.

Mulch, A., Sarna-Wojcicki, A. M., Perkins, M. E., & Chamberlain, C. P. (2008). A Miocene to Pleistocene climate and elevation record of the Sierra Nevada (California). *Proceedings of the National Academy of Sciences*, *105*, 6819–6824.

Newcombe, M. E., Fabbrizio, A., Zhang, Y., Ma, C., Le Voyer, M., Guan, Y., et al. (2014). Chemical zonation in olivine-hosted melt inclusions. *Contributions to Mineralogy and Petrology*, *168*, 1030.

Newman, S., Epstein, S., & Stolper, E. (1988). Water, carbon dioxide, and hydrogen isotopes in glasses from the ca. 1340 AD eruption of the Mono Craters, California: Constraints on degassing phenomena and initial volatile content. *Journal of Volcanology and Geothermal Research*, *35*, 75–96.

Newman, S., & Lowenstern, J. B. (2002). VolatileCalc: A silicate melt–H_2O–CO_2 solution model written in Visual Basic for excel. *Computers in Geoscience*, *28*, 597–604.

Nolan, G. S., & Bindeman, I. N. (2013). Experimental investigation of rates and mechanisms of isotope exchange (O, H) between volcanic ash and isotopically-labeled water. *Geochimica et Cosmochimica Acta*, *111*, 5–27. https://doi.org/10.1016/j.gca.2013.01.020

Peppard, B. T., Steele, I. M., Davis, A. M., Wallace, P. J., & Anderson, A. T. (2001). Zoned quartz phenocrysts from the rhyolitic Bishop Tuff. *American Mineralogist*, *86*, 1034–1052.

Putirka, K., Jean, M., Cousens, B., Sharma, R., Torrez, G., & Carlson, C. (2012). Cenozoic volcanism in the Sierra Nevada and Walker Lane, California, and a new model for lithosphere degradation. *Geosphere*, *8*, 265–291.

Qin, Z., Lu, F., & Anderson, A. T. (1992). Diffusive reequilibration of melt and fluid inclusions. *American Mineralogist*, *77*, 565–576.

Roberge, J., Wallace, P. J., & Kent, A. J. R. (2013). Magmatic processes in the Bishop Tuff rhyolitic magma based on trace elements in melt inclusions and pumice matrix glass. *Contributions to Mineralogy and Petrology*, *165*, 237–257.

Rust, A., Cashman, K., & Wallace, P. (2004). Magma degassing buffered by vapor flow through brecciated conduit margins. *Geology*, *32*, 349–352.

Saal, A. E., Hart, S. R., Shimizu, N., Hauri, E. H., & Layne, G. D. (1998). Pb isotopic variability in melt inclusions from oceanic island basalts, Polynesia. *Science*, *282*, 1481–1484.

Saper L., & Stolper, E. M. (2020). Controlled cooling-rate experiments on olivine-hosted melt inclusions: Chemical diffusion and quantification of eruptive cooling rates on Hawaii and Mars. *Geochemistry, Geophysics, Geosystems*, *21*(2), 1–40. https://doi.org/10.1029/2019GC008772

Sato, T., Funamori, N., Wakabayashi, D., & Nishida, K. T. (2018). Coexistence of two states in optically homogeneous silica glass during the transformation in short-range order. *Physics Review B*, *98*, 144111.

Seaman, S. J., Dyar, M. D., Marinkovic, N., & Dunbar, N. W. (2006). An FTIR study of hydrogen in anorthoclase and associated melt inclusions. *American Mineralogist*, *91*, 12–20.

Seligman, A. N., Bindeman, I., Van Eaton, A., & Hoblitt, R. (2018). Isotopic insights into the degassing and secondary hydration of volcanic glass from the 1980 eruptions of Mount St. Helens. *Bulletin of Volcanology*, *80*, 37. https://doi.org/10.1007/s00445-018-1212-6

Seligman, A. N., Bindeman, I. N., Watkins, J. M., & Ross, A. M. (2016). Water in volcanic glass: From volcanic degassing to secondary hydration. *Geochimica et Cosmochimica Acta*, *191*, 216–238.

Sharp, Z. D., Atudorei, V., & Durakiewicz, T. (2001). A rapid method for determination of hydrogen and oxygen isotope ratios from water and solid hydrous substances. *Chemical Geology*, *178*, 197–210.

Shaw, A. M., Hauri, E. H., Fischer, T. P., Hilton, D. R., & Kelley, K. A. (2008). Hydrogen isotopes in Mariana arc melt inclusions: Implications for subduction dehydration and the deep-Earth water cycle. *Earth and Planetary Science Letters*, *275*, 138–145.

Sieh, K., & Bursik, M. (1986). Most recent eruption of the Mono Craters, eastern central California. *Journal of Geophysical Research*, *91*, 12539–12571.

Skirius, C. M., Peterson, J. W., & Anderson, A. T. (1990). Homogenizing rhyolitic glass inclusions from the Bishop Tuff. *American Mineralogist*, *75*, 1381–1398.

Suzuoki, T., & Epstein, S. (1976). Hydrogen isotope fractionation between OH-bearing minerals and water. *Geochimica et Cosmochimica Acta*, *40*, 1229–1240.

Tartese, R., Anand, M., Barnes, J. J., Starkey, N. A., Franchi, I. A., & Sano, Y. (2013). The abundance, distribution, and isotopic composition of hydrogen in the Moon as revealed by basaltic lunar samples: Implications for the volatile inventory of the Moon. *Geochimica et Cosmochimica Acta*, *122*, 58–74. https://doi.org/10.1016/j.gca.2013.08.014

Taylor, B. E., Eichelberger, J. C., & Westrich, H. R. (1983). Hydrogen isotopic evidence of rhyolitic magma degassing during shallow intrusion and eruption. *Nature*, *306*, 541.

Urakawa, S., Inoue, T., Hattori, T., Sano-Furukawa, A., Kohara, S., Wakabayashi, D.,et al. (2020). X-ray and neutron study on the structure of hydrous SiO_2 glass up to 10 GPa. *Minerals*, *10*, 84.

Venugopal, S., Moune, S., Williams-Jones, G., Druitt, T., Vigouroux, N., Wilson, A., & Russell, J. K. (2020). Two distinct mantle sources beneath the Garibaldi Volcanic Belt: Insight from olivine-hosted melt inclusions. *Chemical Geology*, *532*, 119346.

Wallace, P. J., Anderson, A. T. Jr, & Davis, A. M. (1995). Quantification of pre-eruptive exsolved gas contents in silicic magmas. *Nature*, *377*, 612.

Wallace, P. J., Anderson, A. T. Jr, & Davis, A. M. (1999). Gradients in H_2O, CO_2, and exsolved gas in a large-volume silicic magma system: Interpreting the record preserved in melt inclusions from the Bishop Tuff. *Journal of Geophysical Research*, *104*, 20097–20122.

Wallace, P. J., Dufek, J., Anderson, A. T., & Zhang, Y. (2003). Cooling rates of plinian-fall and pyroclastic-flow deposits in the Bishop Tuff: Inferences from water speciation in quartz-hosted glass inclusions. *Bulletin of Volcanology*, *65*, 105–123.

Walowski, K. J., Wallace, P. J., Clynne, M. A., Rasmussen, D. J., & Weis, D. (2016). Slab melting and magma formation beneath the southern Cascade arc. *Earth and Planetary Science Letters*, *446*, 100–112.

Walowski, K. J., Wallace, P. J., Hauri, E. H., Wada, I., & Clynne, M. A. (2015). Slab melting beneath the Cascade Arc driven by dehydration of altered oceanic peridotite. *Nature Geoscience*, *8*, 404.

Watkins, J. M., Manga, M., & DePaolo, D. J. (2012). Bubble geobarometry: A record of pressure changes, degassing, and regassing at Mono Craters, California. *Geology*, *40*, 699–702.

Wilson, C. J., & Hildreth, W. (1997). The Bishop Tuff: New insights from eruptive stratigraphy. *Journal of Geology*, *105*, 407–440.

Wu, Y., Guo, F., Wang, X. C., Wilde, S. A., & Fan, W. (2020). Derivation of Jurassic HIMU-like intraplate basalts from mantle transition zone in South China: New geochemical constraints from olivine-hosted melt inclusion. *Lithos*, *354–355*, 105337.

Yuan, H., Dueker, K., & Stachnik, J. (2010). Crustal structure and thickness along the Yellowstone hot spot track: Evidence for lower crustal outflow from beneath the eastern Snake River Plain. *Geochemistry, Geophysics, Geosystems*, *11*(3), 1–14. https://doi.org/10.1029/2009GC002787

Zhang, Y., Belcher, R., Ihinger, P. D., Wan, L., Xu, Z., & Newman, S. (1997). New calibration of infrared measurement of dissolved water in rhyolitic glasses. *Geochimica et Cosmochimica Acta*, *61*, 3089–3100.

Zhang, Y., & Stolper, E. M., & Ihinger P. D. (1995). Kinetics of the reaction $H_2O + O = 2OH$ in rhyolitic and albitic glasses: Preliminary results. *American Mineralogist*, *80*, 593–612.

Zierenberg, R. A., Schiffman, P., Barfod, G. H., Lesher, C. E., Marks, N. E., Lowenstern, J. B., et al. (2013). Composition and origin of rhyolite melt intersected by drilling in the Krafla geothermal field, Iceland. *Contributions to Mineralogy and Petrology*, *165*, 327–347.